JEM Journal of Experimental Medicine

ARTICLE

Accumulation of long-chain fatty acids in the tumor microenvironment drives dysfunction in intrapancreatic CD8+ T cells

Teresa Manzo[1,2], Boone M. Prentice[3], Kristin G. Anderson[4,5], Ayush Raman[2], Aislyn Schalck[6], Gabriela S. Codreanu[7], Carina B. Nava Lauson[1], Silvia Tiberti[1], Andrea Raimondi[8], Marissa A. Jones[3], Michelle Reyzer[3], Breanna M. Bates[4,5], Jeffrey M. Spraggins[3], Nathan H. Patterson[3], John A. McLean[7], Kunal Rai[2], Carlo Tacchetti[8], Sara Tucci[10], Jennifer A. Wargo[2,11], Simona Rodighiero[1], Karen Clise-Dwyer[9], Stacy D. Sherrod[7], Michael Kim[11], Nicholas E. Navin[6], Richard M. Caprioli[3], Philip D. Greenberg[4,5], Giulio Draetta[2], and Luigi Nezi[1,2]

CD8+ T cells are master effectors of antitumor immunity, and their presence at tumor sites correlates with favorable outcomes. However, metabolic constraints imposed by the tumor microenvironment (TME) can dampen their ability to control tumor progression. We describe lipid accumulation in the TME areas of pancreatic ductal adenocarcinoma (PDA) populated by CD8+ T cells infiltrating both murine and human tumors. In this lipid-rich but otherwise nutrient-poor TME, access to using lipid metabolism becomes particularly valuable for sustaining cell functions. Here, we found that intrapancreatic CD8+ T cells progressively accumulate specific long-chain fatty acids (LCFAs), which, rather than provide a fuel source, impair their mitochondrial function and trigger major transcriptional reprogramming of pathways involved in lipid metabolism, with the subsequent reduction of fatty acid catabolism. In particular, intrapancreatic CD8+ T cells specifically exhibit down-regulation of the very-long-chain acyl-CoA dehydrogenase (VLCAD) enzyme, which exacerbates accumulation of LCFAs and very-long-chain fatty acids (VLCFAs) that mediate lipotoxicity. Metabolic reprogramming of tumor-specific T cells through enforced expression of *ACADVL* enabled enhanced intratumoral T cell survival and persistence in an engineered mouse model of PDA, overcoming one of the major hurdles to immunotherapy for PDA.

Introduction

The advent of immunotherapy has revolutionized cancer treatment by inducing, providing, and/or reactivating antitumor T cells. Therapeutic results have been heterogeneous, with better outcomes generally correlating with the ability of tumor-specific T cells to infiltrate the tumor, persist, and retain effector functions. Complete and durable clinical responses have been achieved in patients whose cancers were resistant to available standard treatments (Mellman et al., 2011). Yet, it has met with limited success in most patients with solid tumors (Joyce and Fearon, 2015; Menon et al., 2016), including pancreatic ductal adenocarcinoma (PDA; Guo et al., 2017). Although the overall survival rate in PDA patients appears to correlate with CD8+ T cell infiltration (Ene-Obong et al., 2013; Fukunaga et al., 2004; Ino et al., 2013), our knowledge of the mechanisms that regulate the function of these infiltrating T cells in the context of the tumor microenvironment (TME) is still limited.

CD8+ T cells are key effectors of antitumor immunity. However, tumor-infiltrating CD8+ T cells often acquire an altered state of differentiation referred to as "exhaustion" (Wherry and Kurachi, 2015) and, as a result, fail to control tumor outgrowth. Several studies in both murine models of pancreatic cancer and PDA patients have demonstrated that CD8+ T cells are often scarce and, if present, have become dysfunctional (Bailey et al., 2016; Beatty et al., 2015; Clark et al., 2007; Stromnes et al.,

[1]Department of Experimental Oncology, IRCCS European Institute of Oncology, Milano, Italy; [2]Department of Genomic Medicine, The University of Texas MD Anderson Cancer Center, Houston, TX; [3]Department of Biochemistry, Mass Spectrometry Research Center, Department of Chemistry, Department of Pharmacology and Medicine, Vanderbilt University, Nashville, TN; [4]Clinical Research Division and Program in Immunology, Fred Hutchinson Cancer Research Center, Seattle, WA; [5]Departments of Medicine/Oncology and Immunology, University of Washington School of Medicine, Seattle, WA; [6]Department of Genetics and Department of Bioinformatics and Computational Biology, The University of Texas MD Anderson Cancer Center, Houston, TX; [7]Center for Innovative Technology, Vanderbilt University, Nashville, TN; [8]Experimental Imaging Center, IRCCS San Raffaele Scientific Institute, San Raffaele Vita-Salute University, Milano, Italy; [9]Department of Stem Cell Transplantation, The University of Texas MD Anderson Cancer Center, Houston, TX; [10]Laboratory of Clinical Biochemistry and Metabolism Center for Pediatrics and Adolescent Medicine, University of Freiburg, Freiburg, Germany; [11]Department of Surgical Oncology, The University of Texas MD Anderson Cancer Center, Houston, TX.

Correspondence to Luigi Nezi: luigi.nezi@ieo.it; Teresa Manzo: teresa.manzo@ieo.it; B.M. Prentice's present address is Department of Chemistry, University of Florida, Gainesville, FL; A. Raman's present address is Broad Institute of MIT and Harvard, Cambridge, MA.

2015). These observations are perceived to reflect, at least in part, the unique immunosuppressive TME of PDA.

The metabolic state and nutrient availability in the TME are among the main contributing determinants of the functional fate of CD8⁺ T cells infiltrating solid tumors (Wei et al., 2017). Indeed, recent findings suggested that CD8⁺ T cell activation and differentiation are tightly intertwined with metabolic reprogramming. Resting CD8⁺ T cells rely on oxidative phosphorylation (OXPHOS) to fuel their metabolic needs. Upon activation, CD8⁺ T cells engage glycolysis to fulfill their energetic and biosynthetic demands. In contrast, tumor cells are highly glycolytic and support their overgrowth by consuming large amounts of key nutrients, especially glucose (Vander Heiden et al., 2009), which are also required for optimal T cell activation (Siska and Rathmell, 2015). When deprived of glucose, CD8⁺ T cells are compromised in their ability to produce effector cytokines (Cham et al., 2008; Cham and Gajewski, 2005; Jacobs et al., 2008). However, they can still sustain their proliferation and effector functions via mitochondrial OXPHOS (Chang et al., 2015; Sena et al., 2013), using long-chain fatty acids (LCFAs) to fuel the tricarboxylic acid cycle through the process of fatty acid (FA) β-oxidation (FAO) as an alternative to glucose-derived pyruvate, thereby maximizing production of energy and reducing equivalents (Zhang et al., 2017). Therefore, to mount an effective antitumor response, tumor-infiltrating CD8⁺ T cells must retain the metabolic flexibility to adjust in response to the availability of nutrients. It remains unclear how nutrient compositional changes in the TME correlate with the observed dysfunction of tumor-infiltrating CD8⁺ T cells. In a preclinical mouse model of PDA as well as in human tumor specimens, we show that PDA progression is characterized by enrichment of specific lipid accumulation in the TME. In such a lipid-rich TME, intrapancreatic CD8⁺ T cells become exhausted and reduce their ability to metabolize the available lipid substrates. Moreover, the combination of increased lipid levels and decreased mitochondrial function and FAO is toxic to intrapancreatic CD8⁺ T cells, resulting in increased cell death. Our data suggest that metabolic reprogramming of tumor-specific CD8⁺ T cells might represent a strategy to promote survival in the metabolically hostile TME as part of an approach to enhance the clinical efficacy of immunotherapy.

Results

The pancreatic TME accumulates lipid during PDA progression

In PDA, the TME is known to be highly immunosuppressive, limiting T cell infiltration and functions (Liyanage et al., 2002; Mukherjee et al., 2001). Most solid tumors have been reported to be deprived of crucial metabolites needed for T cell function (Ecker and Riley, 2018). To address whether compositional changes in PDA TME might directly contribute to CD8⁺ T cell impairment, we characterized the TME in the KC mouse model, which closely recapitulates human PDA progression (Hingorani et al., 2003). Cohorts of mice were sacrificed at different time points between 9 and 30 wk of age and, based on cytological and architectural abnormalities, divided into early stage of tumor development with pancreatic intraepithelial neoplasia (early PanIN) versus high-grade preneoplastic lesions (late PanIN; Fig. S1 A). Staining of tissue sections revealed that neutral lipids accumulate in the pancreatic tissue during the progression from early to late PanIN, detected with both red oil staining (Fig. S1 B, red arrowheads) and LipidTOX (Fig. S1 C). Therefore, to analyze low molecular weight compounds, we performed a temporally and spatially resolved compositional analysis of the TME by combining confocal imaging on longitudinal samples with a high-resolution, label-free, imaging mass spectrometry (MS) approach (namely high-resolution matrix-assisted laser desorption/ionization Fourier transform ion cyclotron resonance imaging MS, or MALDI FT-ICR IMS, hereafter referred to as IMS). Frozen pancreata were sectioned on a gold-coated stainless-steel target for IMS. IMS was performed in either positive or negative ion mode, generating a mass spectrum at each pixel. Thus, a mean spectrum was generated by segmenting the data through *k*-means clustering and positive correlation with CD8⁺ T cell distribution on consecutive sections upon coregistering the IMS with the confocal images. The peak list of each segment was then searched against the LIPID MAPS database, and mean intensity values for each accurate mass lipid identification were extracted and filtered to retain only those lipids with sufficient signal-to-noise ratios and that represented large fold changes between time points. Finally, data were visualized in a heatmap format sorted by head group, fatty acyl chain length, and level of fatty acyl chain unsaturation (Fig. S1, D and E). This technology has been used previously to survey pancreatic cancer imaging MS to discriminate breast from pancreatic cancer metastasis in formalin-fixed, paraffin-embedded tissues (Casadonte et al., 2014; Eberlin et al., 2014; Grüner et al., 2012) and to survey the molecular composition of multifunctional tissues such as the pancreas (Prentice et al., 2019), but not to characterize the metabolic state (Caprioli et al., 1997; Cornett et al., 2008). Fig. 1 A shows the IMS profiles (right panels) of one representative lipid species, PE(42:6) (a polyunsaturated phosphatidylethanolamine with a total carbon FA chain length of 42 carbons), which was found to be enriched during progression in the areas (one of which is highlighted in orange) populated by CD8⁺ T cells (Fig. 1 B, right panels, insets showing magnifications of the areas highlighted in magenta). Overall, our study revealed, in the areas populated by infiltrating CD8⁺ T cells, an enrichment of specific glycerophospholipids containing very-long-chain FAs (VLCFAs) in PanINs. Results of the global glycerophospholipids analysis are summarized in bar plots representing the relative fraction of lipids of the indicated total carbon FA chain length detected at indicated time points (Fig. 1, C and D; and Fig. S1, F–H). We detected predominantly an increase of PEs and phosphatidylinositols (PIs; Fig. 1, C and D, respectively, with dotted lines highlighting an ∼10% increase), and enrichment of specific species was already evident in early lesions (Fig. 1, E and F; and Fig. S1 E). Global differences were less apparent for phosphatidylserines (Fig. S1 F) and phosphatidylcholines (PCs; Fig. S1 G). Very-long-chain (VLC) sphingomyelins, by contrast, were relatively decreased at late disease time points compared with control (Fig. S1 H).

Quantification of the extracellular glucose in pancreata using a colorimetric assay followed by normalization against the

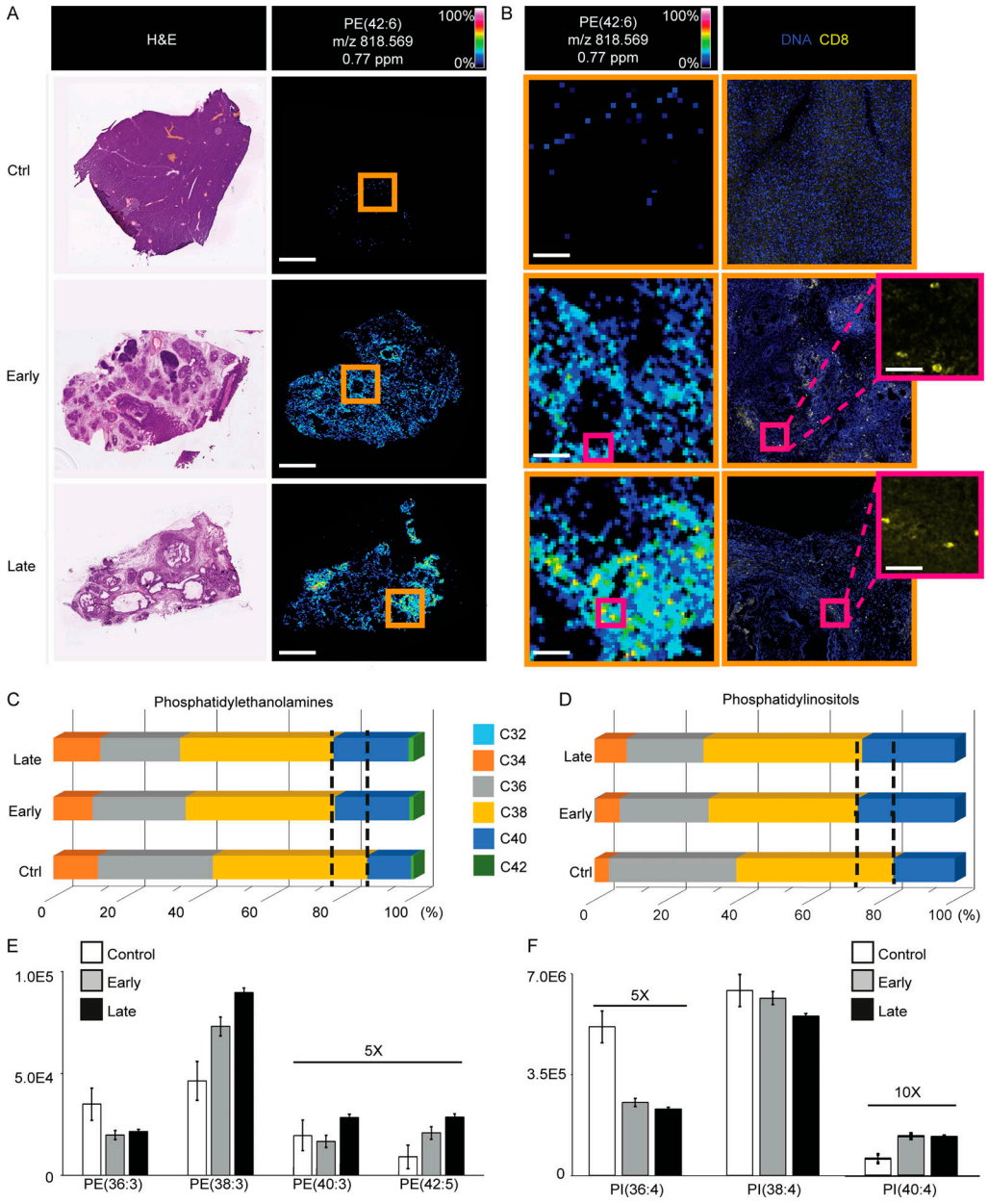

Figure 1. **Neutral lipids and LC glycerophospholipids accumulate in the TME during PDA progression. (A)** Spatial analysis of the pancreatic microenvironment by IMS (right panels, false-color rainbow images displayed without normalization) coregistered with consecutive tissue sections stained with H&E (left panel) at indicated time points (n = 2). Scale bar = 2 mm. **(B)** Spatial analysis of the pancreatic microenvironment by IMS (left panels) coregistered with CD8 T cell localization as detected by confocal imaging on consecutive tissue sections (right panels). IMS intensity distributions show that PEs with LCFAs (left panel, false-color rainbow images displayed without normalization) are colocalized with CD8⁺ T cells (yellow). Nuclei (blue) were stained with DAPI. Representative images (orange quadrants) are sixfold magnifications of the areas indicated in A at the respective time points (n = 2). Insets in the right panels (magenta quadrants) show CD8⁺ T cells at the indicated areas at fourfold magnification. Scale bar = 300 µm; inset = 70 µm. **(C and D)** Bar plots showing the relative fraction of lipids of various FA chain length detected at the different disease time points for PE (C) and PI (D) lipids (FAs for the two lipid types were summed together here, except for PI(38:4), which had an extreme intensity that distorted the bar plot). Dotted lines highlight differences in longer lipid species. **(E and F)** Quantification of IMS data for the indicated selected species inside the PE (E) and PI (F) classes. Y axes indicate intensity. The representation reflects the heterogeneity of selected lipids within each disease time point. Data are expressed as mean ± SE. Intensities for some of the species were multiplied as indicated.

weight of each pancreas highlighted a decrease in glucose availability in late PanINs (Fig. S1 I), suggesting that infiltrating CD8⁺ T cells are restricted to the available long-chain (LC) and VLC glycerophospholipids for fulfilling their metabolic needs in the TME. This model was further supported by the IMS analysis for the first metabolic intermediate of the glycolytic pathway, hexose-6-phosphate (H6P), which was progressively reduced from Early to late PanINs, indicating a decline of the overall glycolytic activity (Fig. S1 J). Altogether, these data suggest that PDA progression is accompanied by distinctive compositional

alterations of the TME that may subvert the metabolic needs of infiltrating CD8⁺ T cells.

CD8⁺ T cells become functionally impaired during PDA progression

Next, we sought to understand whether the compositional changes leading to a lipid-rich but otherwise nutrient-poor TME had an impact on CD8⁺ T function. First, we conducted a longitudinal analysis of the T cell infiltration both in situ, using immunohistochemistry (Fig. 2, A and B), and ex vivo, by flow cytometry of isolated T cells (Fig. 2, C and D). We found that both CD4⁺ (Fig. 2 A, upper panels) and CD8⁺ (Fig. 2 A, lower panels) T cells penetrated into the pancreas at early stages of disease (Fig. 2 A, left panels) and also persisted until late stages (Fig. 2 A, right panels). Flow cytometric analysis of the immune cells infiltrating the pancreatic tissue showed that the percentage of total CD3⁺ T cells peaked at early stages of inflammation (early PanINs) and remained at a similar frequency in high-grade lesions (Fig. 2 D). In line with previous studies (De Monte et al., 2011; McAllister et al., 2014; Stromnes et al., 2015; Zhang et al., 2014), among CD3⁺ T cells, the absolute number of Foxp3⁺ regulatory T cells (T regs; Fig. 2 B) and the percentage of total CD4⁺ T cells (Fig. 2 C) were increased. On the contrary, both absolute number (Fig. 2 B) and frequencies (Fig. 2 C) of CD8⁺ T cells significantly declined over time while they progressively acquired characteristics of functional exhaustion, as indicated by up-regulation of exhaustion markers, including PD1 and TIM3 (Fig. 2, E and F) and reduced ability to produce effector cytokines and molecules such as IFNγ and Granzyme β (Fig. 2, G and H). Thus, PDA is able to recruit an initial CD8⁺ T cell immune response, but the CD8⁺ T cells become functionally impaired during tumor progression.

Intrapancreatic CD8⁺ T cells accumulate VLCFAs

We have described that the glycerophospholipid composition of the TME changes and, concurrently, CD8⁺ T cells infiltrating PDA become progressively dysfunctional. Because T cells can use LCFA to fuel FAO (O'Sullivan et al., 2014; van der Windt et al., 2012), which may be especially useful in a low-glucose environment such as PDA, we queried whether intrapancreatic CD8⁺ T cells effectively acquire free FAs from the external microenvironment. Having found an enrichment in neutral lipids and glycerophospholipids containing VLCFA in the TME, we injected mice i.p. with a fluorescently labeled LCFA (palmitate, Bodipy-C16) and analyzed intrapancreatic CD8⁺ T cells 1 h later by flow cytometry.

Early and late PanINs infiltrating CD8⁺ T cells (in bold gray and black lines, respectively, Fig. 3, A and B) acquired significantly higher amounts of Bodipy-C16 compared with control splenic CD8⁺ T cells (in light gray, Fig. 3, A and B), while the uptake of a fluorescent glucose analogue, 2-[*N*-(7-nitrobenz-2-oxa-1,3-diazol-4-yl)amino]-2-deoxy-D-glucose (2-NBDG), was comparable between CD8⁺ T cell subpopulations (Fig. S2 A). Because FAs can passively cross the cell membrane in a limited extent, we next looked at surface expression of CD36, a receptor that binds LCFAs and facilitates their transport into the cells. We found that a significantly larger population of CD8⁺ T cells sorted from early and late PanINs expressed CD36 on their membrane compared with CD8⁺ T cells sorted from spleen (Fig. S2 B), consistent with an increased uptake of LC lipids by infiltrating CD8⁺ T cells. Of note, we observed higher Bodipy-C16 uptake also in CD4⁺ T cells and total CD45⁺CD3⁻ myeloid cells compared with their splenic counterparts (Fig. S2 C), suggesting a general mechanism by which immune cells infiltrating the pancreatic TME adapt to its peculiar nutrient composition by attempting to switch from a glucose- to a lipid-based metabolism.

To evaluate if and to what extent the nature of the lipid species acquired from the TME could impact the global lipid compositions of T cells, intrapancreatic CD8⁺ and CD4⁺ T cells were flow-sorted from early and late PanINs, and total lipids were analyzed by liquid chromatography–MS. As indicated from principal component analysis (PCA; Fig. S2 D), using abundance levels for all metabolite species across each sample to determine the principal axes of abundance variation, splenic naive T cells and early and late PanINs infiltrating CD8⁺ T cells have different metabolic profiles. Unsupervised clustering of the lipid expression profiles of CD8⁺ T cells revealed that the lipid composition of infiltrating CD8⁺ T cells was already significantly different from naive cells at early time points (Fig. 3 C). However, compared with early stages, CD8⁺ T cells infiltrating late PanINs exhibited even more pronounced compositional changes, with increase (399 and 165 ions detected in positive and negative mode, respectively) or decrease (14 and 106 ions detected in positive and negative mode, respectively) of a large number of lipid species (Fig. S2 E). In particular, annotation of statistically different lipid metabolic compounds over the time course of disease progression confirmed an overall increase of lipids in infiltrating CD8⁺ T cells, which was more marked in late PanINs in the superclass level of the FAs (Fig. S2 G, red column). These compositional changes were peculiar for CD8⁺ T cells infiltrating late PanINs. Indeed, infiltrating CD4⁺ T cells sharing the same TME showed minimal differences in early versus late PanINs (increase of 24 and 25 ions and decrease of 12 and 44 ions in positive and negative mode, respectively; Fig. S2 F), suggesting that, unlike CD8⁺ T cells, CD4⁺ T cells did not experience major lipid accumulation during tumor progression. Accordingly, when comparing the lipid compositional profiles of CD8⁺ and CD4⁺ T cells infiltrating late PanINs, we observed an overall increment of lipids at all superclass levels except glycerophospholipids (Fig. 3 D), which are the main structural components of cellular membranes. The greatest increase involved the FA superclass (Fig. 3 D, FA), and analysis of fold changes of average peak areas of putatively identified FA metabolites in either CD8⁺ or CD4⁺ T cells revealed an enrichment of different FAs at late time points (Fig. 3 E). All these FAs are LC lipids, with chain lengths ranging from C12 to C16. In summary, our lipidomic analysis confirmed that tumor-infiltrating CD8⁺ T cells encounter major changes in their lipid composition and accumulate mostly LCFAs at late stages.

CD8⁺ T cell dysfunction is associated with accumulation of specific LCFAs

We have shown that the pancreatic TME is enriched for LC and VLC glycerophospholipids and that infiltrating CD8⁺ T cells

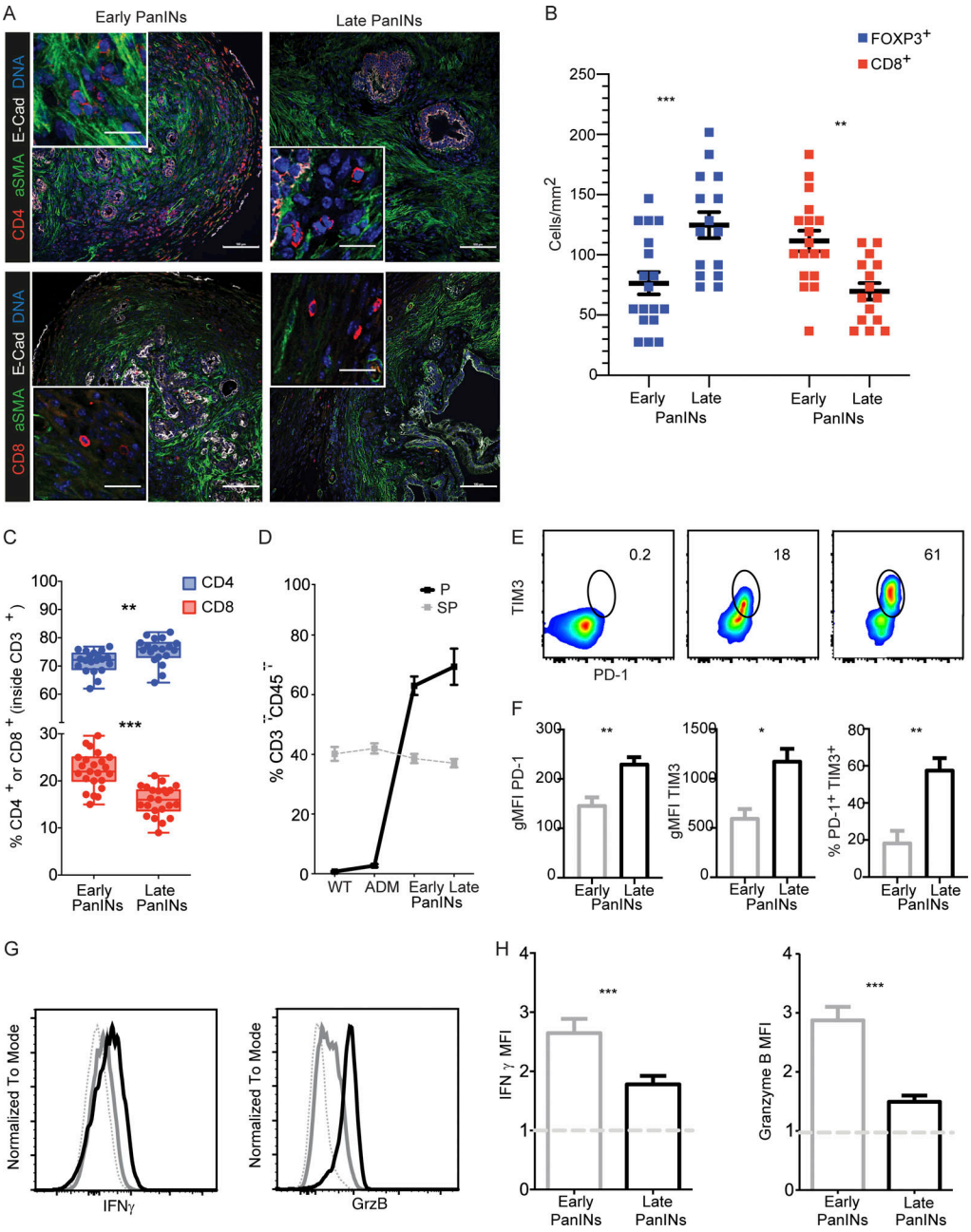

Figure 2. **Intrapancreatic CD8 T cells become functionally impaired during PDA progression. (A)** Confocal images of formalin-fixed, paraffin-embedded murine pancreatic samples displaying CD4+ (upper panels) or CD8+ (lower panels) T cell infiltration in early (left) versus late (right) PanINs. CD4+ or CD8+ (red), aSMA (green) and E-cad (white) were detected by indirect immunofluorescence, and nuclei (blue) were stained with DAPI. Inserts show magnified views of representative subregions. Scale bar = 100 µm; insets = 25 µm. Images are representative of one experiment with three mice in each group. **(B)** Quantification by immunofluorescence of FoxP3+ T reg cells (blue) and CD8+ T cells (red) on pancreata from early versus late PanINs. Results are indicative of at least five different fields on three independent mice. **(C)** Percentages of CD8+ or CD4+ T cells inside CD3+CD45+ gate from pancreata of mice with early and late PanIN lesions (n = 25). **(D)** Kinetic showing infiltration of T cells in spleen (gray) and pancreata (black) at indicated time points. Numbers indicate percentages of CD3+CD45+ cells (n = 25). **(E)** Representative dot plots of intrapancreatic CD8+ T cells expressing the indicated exhaustion markers. WT spleen (left), early (center), and late (right) PanINs are shown. Numbers indicate percentage of CD8+ T cells that are double-positive T cells. **(F)** Quantification of PD1+, TIM3+ or PD1+TIM3+ T cells inside CD3+CD8+ gate from pancreata of mice with early (n = 4) and late (n = 5) PanIN lesions. **(G and H)** Representative histograms (G) and quantification (H) of effector functions of CD8+ T cells infiltrating early (gray, n = 8) and late (black, n = 10) PanINs assessed as IFNγ and Granzyme β production measured by ex vivo intracellular cytokine staining. Results are expressed as MFI and shown as normalized to control splenic CD8+ T cells. In all graphs, error bars represent mean ± SEM. Statistics were calculated using unpaired two-tailed Student's t test; *, P ≤ 0.05–0.01; **, P ≤ 0.01–0.001; ***, P ≤ 0.001–0.0001.

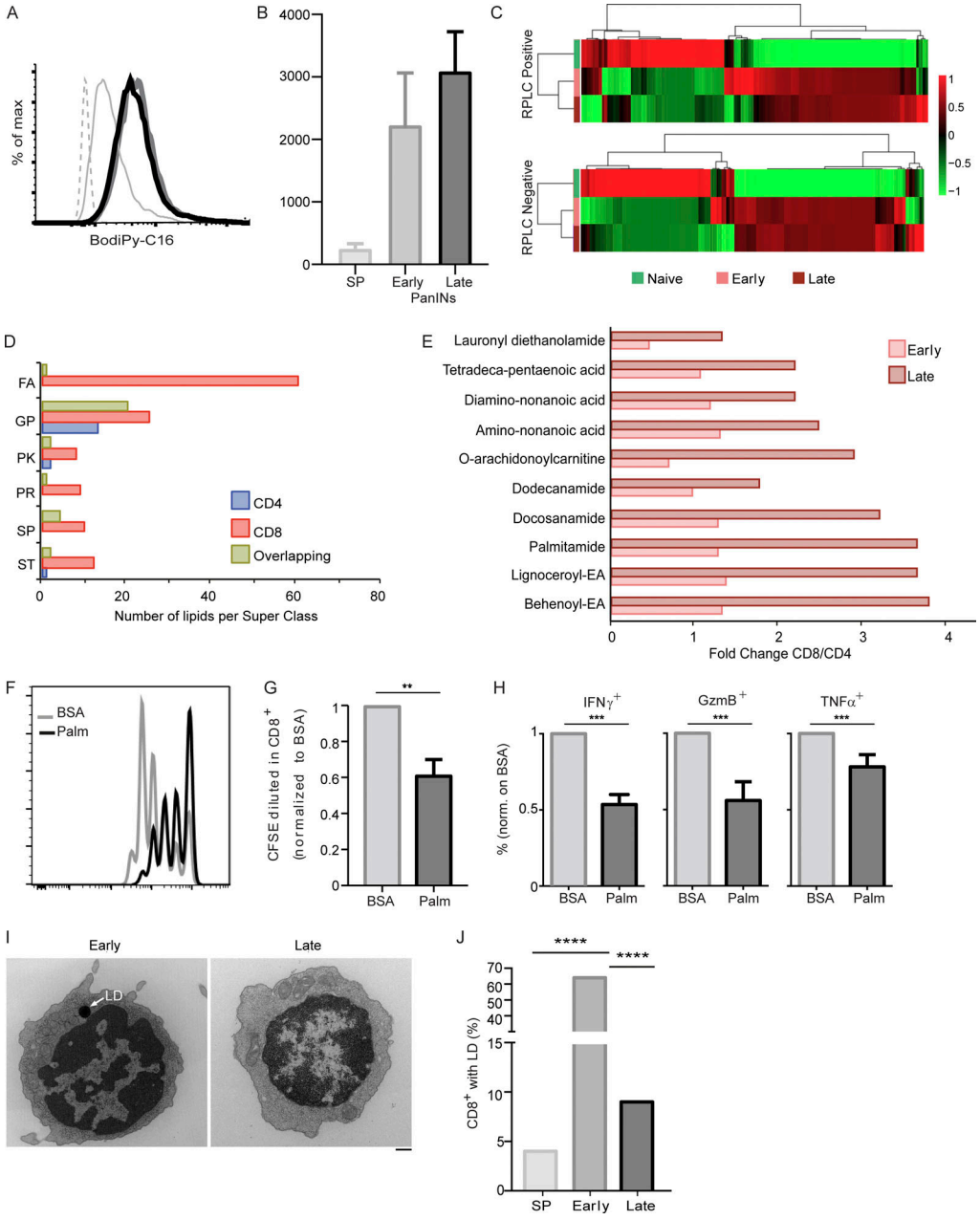

Figure 3. **Intrapancreatic CD8⁺ T cells accumulate VLCFAs. (A)** Representative histogram of in vivo Bodipy-C_{16} uptake in early (bold gray line) and late (bold black line) PanINs infiltrating CD8⁺ T cells compared with control splenic CD8⁺ T cells (gray line). For fluorescence minus one (FMO control), mice were not injected with fluorescent analogous (dotted shaded line). **(B)** Bar graph showing the quantification of the Bodipy-C_{16} MFI. Data are mean of three mice per group and representative of three independent experiments. **(C)** Heatmap providing direct visualization of the relative levels of individual lipids. Samples (columns) are clustered by group average, and rows are colored according to relative feature abundance across different groups, ranging from low (green) to high (red). It was constructed by Metaboanalyst 4.0 software using Pearson average clustering algorithm unsupervised clustering of relative levels of individual lipids (RPLC mode indicated on the left). Color code indicated in the legend. **(D)** Annotation of statistically different lipid metabolic compounds detected in CD4⁺ (blue), CD8⁺ (red), and both (green) T cell types sorted from late PanINs (GP, glycerophospholipids; PK, polyketides; PR, prenols; SP, sphingolipids; ST, sterols). **(E)** Bar graphs showing fold changes of the indicated lipid compounds in CD8⁺ compared with CD4⁺ T cells in early (light red) and late (dark red) PanIN lesions. **(F–H)** T cells activated with αCD3/αCD28 with 100 µM BSA-palmitate (black) or BSA (as control, gray) for 72 h. CFSE profile (F) and bar graph showing the relative quantification of percentage of CFSE diluted cells (G) and IFNγ-, Granzyme β–, and TNFα-producing cells (H) in BSA-palmitate–treated CD8⁺ T cells normalized (norm.) on BSA control cells. Data are representative of 10 independent experiments. **(I)** Representative TEM image of LDs from CD8⁺ T cells infiltrating early (left) and late (right) PanINs. **(J)** Bar graph showing percentage of CD8⁺ T cells containing LDs in FACS-sorted naive (light gray bar), early (dark gray bar), and late (black bar) T cells as determined by TEM analysis. Data are representative of one experiment with ≥100 cells counted in each experimental condition. In all graphs, error bars represent mean ± SEM. Statistics were calculated using a two-tailed Student's *t* test; *, P ≤ 0.05–0.01; **, P ≤ 0.01–0.001; ***, P ≤ 0.001–0.0001; ****, P ≤ 0.0001.

increase their uptake and accumulate LCFAs in high-grade lesions. Therefore, we asked whether an excess of specific LCFAs might contribute to the induction of T cell dysfunction. Having found palmitamide in the list of the FAs that accumulate in CD8⁺ T cells isolated from late PanINs (Fig. 3 E), we cultured CD8⁺ T cells in the presence of BSA-palmitic acid (Palm; palmitamide is a primary FA amide coming from palmitic acid). We found that Palm decreased proliferation (Fig. 3, F and G) and ability to secrete effector molecules such as IFNγ, Granzyme β, and TNFα (Fig. 3 H), mimicking the dysfunctional state of CD8⁺ T cells seen in vivo (Fig. 2, G and H). Of note, neither a medium-chain FA such as hexanoic acid (Fig. S2 H) nor an LCFA such as BSA-linoleic acid, which we did not find to accumulate (Lino; Fig. S2, I and J), had any relevant impact on CD8⁺ T cells in the same experimental setup, supporting the idea that CD8⁺ T dysfunction may be associated with the accumulation of specific lipid metabolites.

An excess of intracellular free FAs is known to damage cellular membranes (Aon et al., 2014), and to limit such cytotoxicity, they are stored in lipid droplets (LDs), which function as both an energetic reservoir and protective mechanism at once (Nguyen and Olzmann, 2017; Thiam and Beller, 2017; Welte, 2015). Although we did see formation of LDs in CD8⁺ T cells treated with Lino, we observed a significant defect in LD accumulation after Palm treatment, as assessed by both Red Oil and LipidTOX staining (Fig. S2, K and L, respectively), suggesting that this protective mechanism depends on the quality rather than quantity of LCFAs taken up and, in agreement with previous observations (Listenberger et al., 2003; Plötz et al., 2016), does not occur in response to excess palmitate. Based on these observations, we reasoned that effective storage of LCFAs in LDs could also be relevant for limiting lipotoxicity in CD8⁺ T cells infiltrating late PanINs. Therefore, we examined the ability of CD8⁺ T cells to form LDs in vivo during tumor progression. Even though >20% of the CD8⁺ T cells infiltrating early lesions contain LDs, this percentage was significantly reduced at late time points (Fig. 3, I and J; and Fig. S2 M). Altogether, these data suggest that CD8⁺ T cells infiltrating late PanINs have limited capacity to store specific LCFAs in LDs, and this may induce higher lipotoxicity and contribute to their exhaustion.

Intrapancreatic CD8⁺ T cells are metabolically exhausted in the lipid-rich PDA TME

Elevated levels of free FAs are associated with apoptosis in many cell types (Sharma and Alonso, 2014; Ulloth et al., 2003). Moreover, palmitic acid has been reported to directly induce mitochondrial dysfunction (de Pablo et al., 1999), potentially by disrupting the mitochondria-associated ER membrane (Shinjo et al., 2017). We confirmed these findings in our in vitro optimally activated CD8⁺ T cells by looking at the effect of palmitic acid on their mitochondrial function. As expected, CD8⁺ T cells treated with palmitic acid showed decreased mitochondrial functionality (detected as a drop in the mitochondrial potential with MitoTracker Orange CMTMRos staining; Fig. 4 A). Conversely, treatment with linoleic acid did not induce any mitochondrial dysfunction (Fig. 4 B).

Because mitochondrial function strictly depends on their structural integrity, we employed transmission EM (TEM) to assess the state of mitochondria based on morphology in intrapancreatic CD8⁺ T cells sorted from early and late PanINs. CD4⁺ T cells from the same animals were used as a control population experiencing the same hostile TME. Morphometric analysis revealed that intrapancreatic CD8⁺ T cells experienced severe mitochondrial defects. These abnormalities were more pronounced than in CD4⁺ T cells and were already evident in cells infiltrating early PanINs but worsened during disease progression (Figs. 4, C and D). Indeed, CD8⁺ T cells infiltrating late PanINs displayed higher frequencies of mitochondria with irregular cristae and dilated intercrista spaces (swollen), as well as hypercondensed mitochondria with a distinct electron dense matrix (Fig. 4, C and D), which are usually found in preapoptotic cells (Green and Reed, 1998). Together with decreased mitochondrial mass (as assessed by MitoTracker Green FM; Fig. 4 E) and functionality (Fig. 4 F), these results highlight a severe mitochondrial impairment in CD8⁺ T cells infiltrating late PanINs and support the hypothesis that accumulated lipids may have a detrimental impact on mitochondrial integrity in these cells.

To address causality between uptake of specific LC lipids and acquired mitochondrial dysfunction, we activated CD8⁺ T cells in vitro in the presence of Palm or Lino and assessed mitochondrial integrity (MitoTracker⁺) in the cells accumulating LC lipids (Bodipy FL C_{16}⁺). As predicted, in the fraction of CD8⁺ T cells accumulating Bodipy FL C_{16}⁺, mitochondrial staining significantly decreased only upon Palm treatment (Fig. 4 G). Because CD8⁺ T cells accumulating neutral lipids (LipidTOX⁺) did not show similar mitochondrial defects even upon Palm treatment (Fig. 4 H), we concluded that mitochondrial defects tightly correlated with the type of lipid taken up and the ability to form LDs.

This link was further validated in vivo in tumor-infiltrating CD8⁺ T cells. Indeed, we injected Bodipy FL C_{16}, isolated CD8⁺ T cells from the tumor, and stained with MitoTracker Orange CMTMRos. This allowed us to track in vivo T cell lipid uptake and concurrently assess mitochondrial function. FACS analysis revealed a significantly higher frequency of Bodipy FL C_{16}–positive and MitoTracker-negative cells in the CD8⁺ compartment (in red) compared with the CD4⁺ compartment (in blue; Figs. 4, I and J). These results suggested that, although most CD4⁺ T cells could tolerate the uptake of LC lipids, a large fraction of the CD8⁺ T cells taking up LC lipids bore damaged mitochondria. Similar results were obtained when comparing CD8⁺ T cells with the myeloid cell compartment (CD45⁺ CD3⁻; Fig. 4 J), suggesting that lipid accumulation and mitochondrial dysfunction could be intertwined specifically within infiltrating CD8⁺ T cells.

Because T cells have to rely on mitochondrial OXPHOS to use lipids as an energy source, we predicted that the severe mitochondrial dysfunction experienced by CD8⁺ T cells infiltrating late PanINs could have an impact on their bioenergetic profile. Thus, we analyzed the metabolic flux of infiltrating CD8⁺ and CD4⁺ T cells sorted from early and late PanINs in real time using an extracellular flux analyzer (Seahorse XF Analyzers), which monitors the O_2 consumption rate (OCR) as an indicator of OXPHOS and the extracellular acidification rate (ECAR) as a readout for glycolysis. As expected, T cells (both CD4⁺ and CD8⁺)

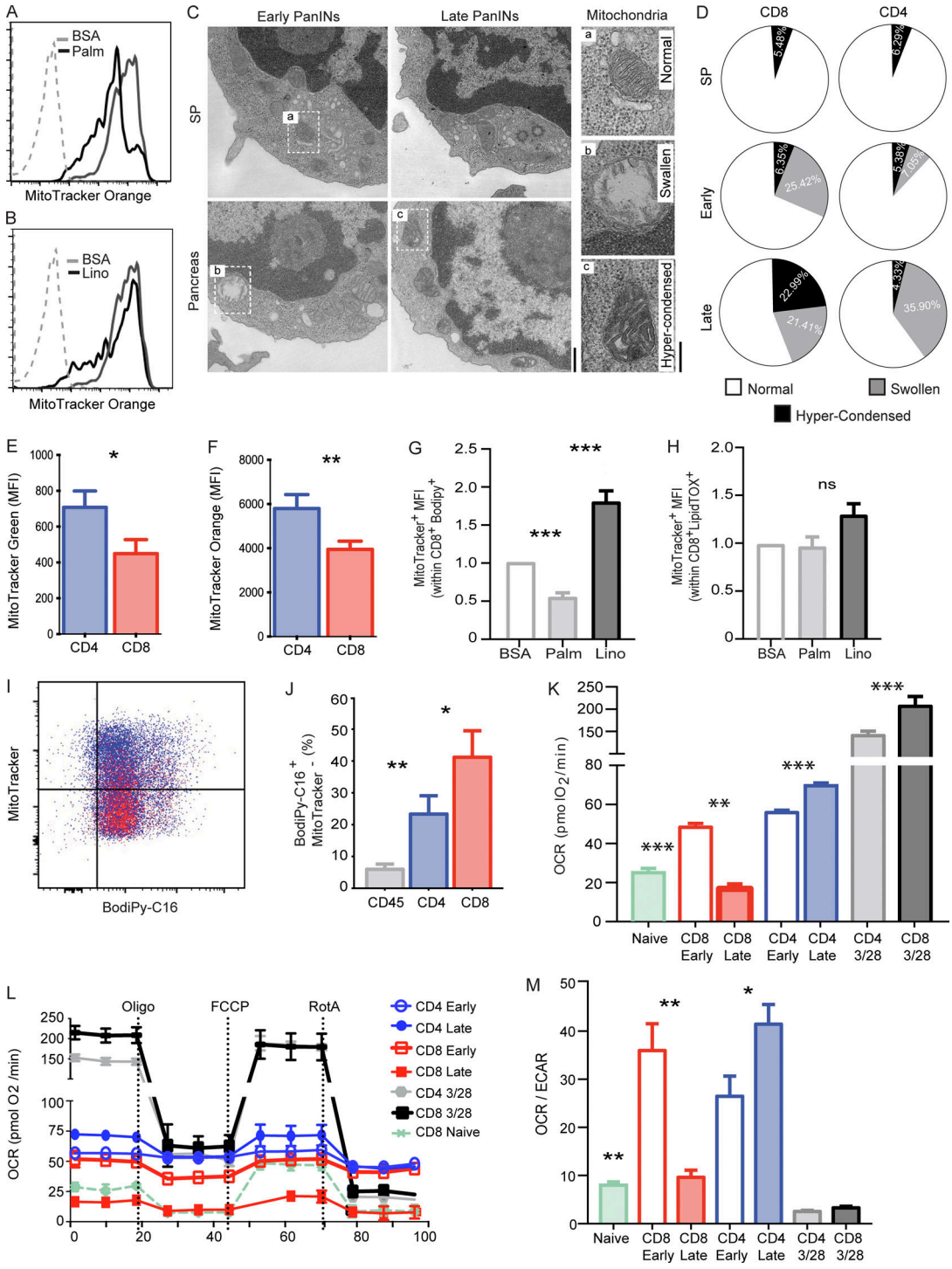

Figure 4. **Intrapancreatic CD8⁺ T cells are metabolically exhausted in the lipid-rich PDA TME. (A and B)** Representative histogram of MitoTracker Orange CMTMRos performed on αCD3/αCD28 activated CD8⁺ T cells in the presence of palmitic (A, *n* = 15) or linoleic (B, *n* = 15) acid. Control BSA-treated cells are indicated in gray (*n* = 15). Dotted light gray line represents fluorescence minus one (FMO control). **(C)** TEM of CD8⁺ and CD4⁺ T cells FACS sorted from spleen or early and late PanIN lesions. Representative image of TEM on CD8⁺ T cells from the indicated organ and time points. Inserts show magnification of representative normal (a), swollen (b), and hypercondensed (c) mitochondria. **(D)** Pie chart showing the results of mitochondrial morphometric analysis of CD4⁺ and CD8⁺ T cells from spleen and early and late PanIN lesions. Grading from normal (white) to swollen (gray) and hypercondensed (black) follows worsening of abnormalities (see Materials and methods for details). Numbers indicate percentages of the relative grading per cell. Data are from one experiment with ≥50 cells per group. **(E and F)** Bar graphs showing quantification of MitoTracker Green (E, *n* = 7) and MitoTracker Orange CMTMRos (F, *n* = 17) from CD8⁺ (red) or CD4⁺ (blue) T cells infiltrating late PanINs. Numbers indicate MFI. **(G and H)** Bar graphs showing mitochondrial staining in BodiPy-C_{16}⁺ (G) or LipidTOX⁺ (H) on CD8⁺ T cells activated in the presence of palmitic (*n* = 8) or linoleic (*n* = 8) acid. Results show Mitotracker MFI normalized on BSA-treated cells used as a control (*n* = 8). **(I)** Representative overlay of dot plot for CD8⁺ (red) and CD4⁺ (blue) T cells showing in vivo BodiPy-C_{16} uptake and mitochondrial function measurements. **(J)** Bar graphs show percentages of BodiPy-C_{16}–positive and MitoTracker Orange CMTMRos–negative cells gated on CD8⁺ (red) and

CD4+ (blue) T cells or CD45+/CD3− (gray) cells from late PanINs (n = 6). **(K–M)** Real-time analysis of OXPHOS (L) and quantification of OCR (K) and ratio of OCR to ECAR in T cells (M) on CD8+ (red) and CD4+ (blue) T cells sorted from early (n = 3) and late (n = 3) PanINs measured in a Seahorse extracellular flux analyzer. Naive and T cells activated for 48 h with αCD3/αCD28 antibodies are included as control (n = 8, green and gray bars, respectively). In all graphs, error bars represent mean ± SEM. Statistics were calculated using a two-tailed Student's t test; *, P ≤ 0.05–0.01; **, P ≤ 0.01–0.001; ***, P ≤ 0.001–0.0001; ns, not significant.

after activation with CD3/CD28 ligation dramatically increased OCR compared with naive T cells (Fig. 4, K and L), but preferentially used aerobic glycolysis (lower OCR/ECAR ratio; Fig. 4 M). By contrast, OXPHOS was vital for early infiltrating CD8+ and CD4+ T cells, as indicated by their increased OCR (Fig. 4, K and L) and OCR/ECAR ratio (Fig. 4 M) compared with resting naive T cells, likely as a means to meet the high metabolic demand necessary to exert their function within the tumor. However, CD8+ T cells progressively lost their ability to engage OXPHOS, as demonstrated by the significantly lower OCR (Fig. 4, K and L, red column) and OCR/ECAR ratio (Fig. 4 M, red column) at late time points compared with cells in early PanINs. In contrast, infiltrating CD4+ T cells increased OCR rate during tumor progression (Figs. 4, K and L, blue column), and the frequency of CD4+ T cells increased over time (Fig. 2 C). These data suggested that, unlike CD4+ cells, CD8+ T cells cannot adapt to the lipid-rich TME by switching their metabolism from glycolysis to OXPHOS. Together, our data show that the lipid-rich TME is populated with metabolically defective CD8+ T cells, which fail to effectively engage the OXPHOS pathway in response to limited glycolysis, an obligate step to sustain viability and exert effector functions.

CD8+ T cells infiltrating late PanINs show ACADVL down-regulation

To probe the mechanistic details of the metabolic dysfunction in intrapancreatic CD8+ T cells infiltrating late PanINs, we profiled the transcriptome of flow-sorted intrapancreatic CD8+ T cells. RNA sequencing (RNA-seq) highlighted distinct signatures associated with early and late PanINs. In particular, PCA (Fig. S3 A) and unsupervised clustering (Fig. 5 A) of expression profiles showed that infiltrating CD8+ T cells isolated from late PanINs were transcriptionally distinct from those isolated from the early PanINs. Compared with CD8+ T cells isolated from early PanIns, cells isolated from late lesions were characterized by down-regulation of key genes involved in cell-mediated cytotoxicity (orange dots, *Gzma* and *Gzmb*) and mitochondrial function (blue dots, *Ndufa3*, *Ndufa9*, *Ndufa11*, and *Vdac3*; Fig. 5 B), consistent with what we observed studying phenotypes. Moreover, there was up-regulation of genes involved in peroxisome biogenesis (*Pex11g* and *Pex13*) and ER stress (*Atf6*, *Txndc11*, and *Txndc12*; magenta dots, Fig. 5 B). Furthermore, gene set enrichment analysis (GSEA) of significantly differentially regulated genes demonstrated altered metabolic signatures in the different T cell populations, including gene subsets associated with FA homeostasis (Figs. S3 B).

Among these genes, the transcriptional down-regulation of the VLC acyl-CoA dehydrogenase (*ACADVL*) caught our attention, because this enzyme catalyzes the initial step of mitochondrial β-oxidation and targets esters of LCFAs and VLCFAs (with a chain length of 12–20 carbons; Tucci et al., 2012), which we had initially found to be accumulated in the areas infiltrated by CD8+ T cells during tumor progression.

Thus, we employed quantitative confocal microscopy to validate ACADVL down-regulation at protein levels. Enzyme levels were measured as mean fluorescence intensity (MFI) inside each T cell, and specific antibodies targeting CD8+ (Fig. 5 C) or CD4+ (Fig. 5 D) cells were used to distinguish between the two subpopulations at early and late time points (Fig. 5, C and D, left and right panels, respectively). Our analysis confirmed that CD8+ T cells had lower levels of VLC acyl-CoA dehydrogenase (VLCAD) when infiltrating late PanINs compared with early (as highlighted by differences in the number of yellow merged cells in Fig. 5 C compared with Fig. 5 D, and in the MFI in Fig. 5 E). By contrast, in the same lipid-rich TME, CD4+ T cells did up-regulate the level of VLCAD (Fig. 5, D and E), consistent with their ability to engage OXPHOS and adapt to the changing TME.

To investigate whether the accumulation of specific LCFAs in the TME was sufficient to induce the observed transcriptional changes, we assayed the expression of a subset of genes (n = 84) involved in the regulation and enzymatic pathways of FA metabolism in CD8+ T cells activated in vitro in the presence of palmitic or linoleic acid. In agreement with previous findings, we found that activated CD8+ T cells differentially regulate a large fraction (n = 58) of the tested genes compared with resting naive T cells (Fig. S3, C and D, left panel). However, the activation in the presence of Palm substantially changed their transcriptional profile (n = 54; Fig. S3, C and D, central panel), in particular of genes involved in FA metabolism. This recapitulates the changes observed in the RNA-seq analysis of flow-sorted infiltrating CD8+ T cells (Fig. 5, A and B). Interestingly, CD8+ T cells responded similarly to treatment with either Lino or Palm (Fig. S3, C and D, right panel), revealing a general transcriptional response to the excess of LCFAs. Of note, ACADVL was significantly down-regulated in LCFA-treated cells compared with control (Fig. S3, C and E), confirming that its expression is tightly dependent on LCFA accumulation.

Altogether, our data indicate that CD8+ T cells undergo major transcriptional changes after entering the TME, which involve down-regulation of mitochondrial function and lipid homeostasis in response to lipid accumulation. In the peculiar PDA TME, which is enriched in lipids containing LCFAs, the down-regulation of ACADVL is particularly relevant, because it impairs the ability of CD8+ T cells to metabolize the excess of specific LCFA lipids, amplifying their cytotoxic effect.

Tumor-specific T cells engineered to express higher levels of ACADVL exhibit enhanced metabolic fitness

To evaluate whether enforcing overexpression of ACADVL has the potential to enhance T cell metabolic fitness in a clinically

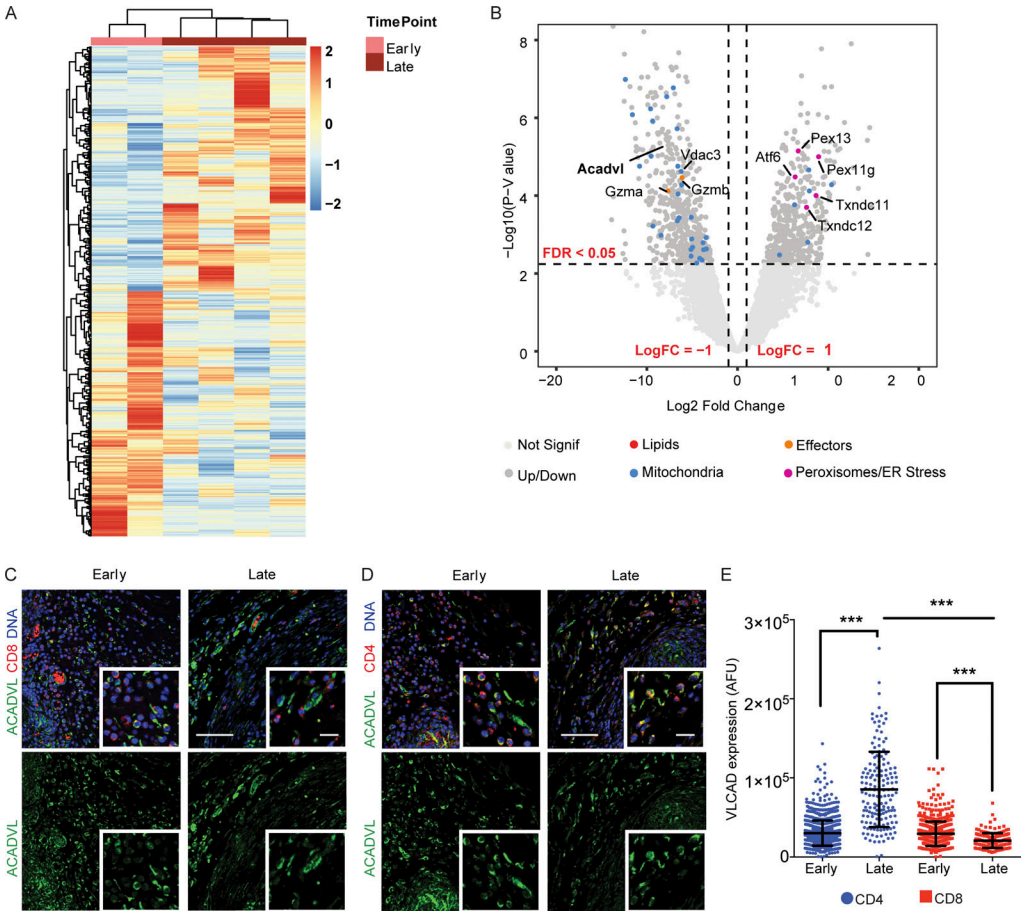

Figure 5. **ACADVL deficiency in CD8⁺ T cells infiltrating late PanINs. (A)** Unsupervised clustering analysis of the transcriptome of intrapancreatic CD8⁺ T cells flow sorted from WT or KC mice at indicated ages (n = 3; see legend for color code). Top 3,000 most variable genes were used to plot the heatmap. **(B)** Volcano plot showing genes differentially regulated in CD8⁺ T cells infiltrating late versus early PanINs. Significantly differentially regulated genes related to lipid (red), mitochondria (blue), and peroxisomes/ER stress (magenta) are highlighted. Comparison between 30- and 13-wk samples; with absolute log2 fold change > 1 and false discovery rate (FDR) < 0.05. **(C and D)** Representative confocal images of multicolor immunofluorescence staining displaying ACADVL expression in CD8⁺ (C) or CD4⁺ (D) T cells infiltrating early (left panels) versus late (right panels) PanINs. ACADVL is in green, CD8⁺ and CD4⁺ T cells in red; nuclei (blue) were stained with DAPI. Scale bar = 100 µm; insets = 20 µm. **(E)** ACADVL expression quantification shown as arbitrary fluorescence unit (AFU). Each dot represents one cell, and the expression level of ≥50 cells per condition were quantified on three independent samples using a built-in NIS Element tool. Error bars represent mean ± SEM. Statistics were calculated using a two-tailed Student's t test; ***, P ≤ 0.001–0.0001.

relevant model, CD8⁺ T cells, transduced to express a high-affinity TCR (designated TCR_{1045}) specific for mesothelin (Msln), a protein tumor target overexpressed by human and murine PDA cells, were additionally engineered to also overexpress ACADVL. We transduced CD8⁺ T cells with a construct containing either TCR_{1045} alone or TCR_{1045} and ACADVL linked by a P2A element to ensure equimolar expression (Fig. 6 A). Transduced T cells expressed the engineered TCR (Vβ9⁺) and bound H2-D^b tetramers, the presenting MHC I allele, containing $Msln_{406–414}$ (Fig. S4 A). ACADVL overexpression in Msln-specific T cells resulted in elevated enzymatic activity in cells transduced with ACADVL-TCR_{1045} compared with TCR_{1045} alone (Fig. 6 B). We also observed higher mitochondrial function in the T cells overexpressing *ACADVL* (Fig. 6, C and D). Of note, 7 d after in vitro stimulation and transduction, both cell types similarly expressed activation markers CD69 and 4-1BB (Fig. S4 B) and produced similar amounts of the antitumor cytokines IFNγ and TNFα in response to stimulation with the cognate $Msln_{406–414}$ peptide (Fig. S4 C).

To assess the effect of ACADVL overexpression on the energetic profile of tumor-specific CD8⁺ T cells, Msln-specific T cells were evaluated for changes in OCR and ECAR 7 d after transduction and in vitro stimulation using the Seahorse Mito Stress Test. ACADVL-TCR_{1045} cells exhibited elevated basal OCR and spare respiratory capacity (Fig. 6, E and F) relative to TCR_{1045} T cells. These data suggest that enhanced ACADVL enzymatic activity in CD8⁺ T cells confers enhanced mitochondrial metabolic fitness and ability to respond to mitochondrial stress, which has the potential to improve T cell survival in a metabolically harsh TME, particularly one with excess VLCFAs.

To test this hypothesis, we evaluated the in vivo activity of these metabolically reprogrammed T cells in a model of adoptive T cell therapy (ATC) for genetically engineered PDA in KPC mice. In these mice, infused Msln-specific CD8⁺ T cells have been shown to infiltrate PDA and kill pancreatic tumor cells but to undergo severe contraction in cell number within 3 wk of infusion, and the cells that do persist become progressively

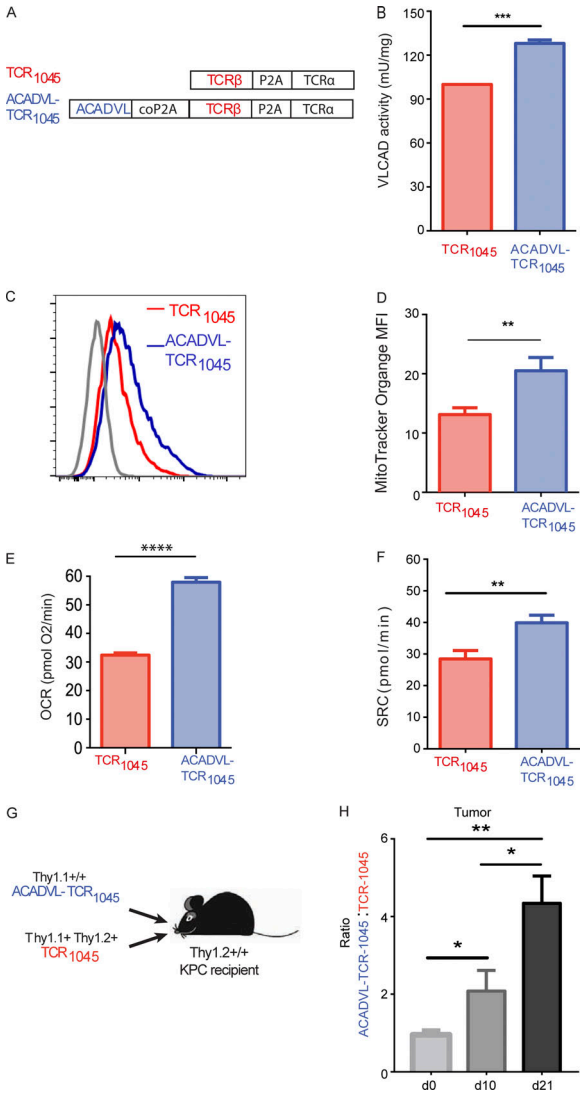

Figure 6. **Tumor-specific T cells engineered to express ACADVL are empowered with a better metabolic fitness. (A)** Design of TCR_{1045} and ACADVL-TCR_{1045} constructs. **(B)** Bar graphs show quantification of VLCAD enzymatic activity from TCR_{1045} and ACADVL-TCR_{1045} T cells sorted on live, $CD8^+$ $Thy1.1^+$ $V\beta9^+$ T cells (n = 8). **(C and D)** Representative histogram (C) and bar graphs (D) showing quantification of MitoTracker Orange staining in TCR_{1045} and ACADVL-TCR_{1045} T cells. Data are mean of four independent experiments. **(E and F)** Basal OCR (E) and spare respiratory capacity (the difference between maximal OCR and basal OCR rates, F) were evaluated using Seahorse analysis of TCR_{1045} and ACADVL-TCR_{1045} T cells. The data represent analysis of the results of four experiments using a two-tailed Student's t test. **(G)** Cotransfer schema. Equal numbers of live $CD8^+$ $V\beta9^+$ TCR_{1045} and ACADVL-TCR_{1045} T cells were sorted and transferred into KPC recipient mice harboring at least one pancreatic tumor detectable as 2–5 mm^3 in diameter (measured by ultrasound). **(H)** Ratio of ACADVL-TCR_{1045} to TCR_{1045} $CD8^+$ T cell numbers pretransfer (day 0) and isolated from KPC tumors 10 and 21 d after transfer. Proportions of cotransferred TCR_{1045} T (red) and ACADVL-TCR_{1045} T cells (blue) 21 d after transfer in the tumor, gated on live $CD8^+$ $Thy1.1^+$ cells. Data are from four independent experiments (n = 4 mice per group). In all graphs, error bars represent mean ± SEM. Statistics were calculated using a two-tailed Student's t test; *, P ≤ 0.05–0.01; **, P ≤ 0.01–0.001; ***, P ≤ 0.001–0.0001; ****, P ≤ 0.0001.

dysfunctional, thereby failing to sustain long-term antitumor activity (Stromnes et al., 2015). Therefore, we monitored KPC mice until development of a defined pancreatic tumor mass (usually ∼10–12 wk, assessed by monitoring with serial high-resolution ultrasound imaging) and then adoptively co-transferred equal numbers of TCR_{1045} and ACADVL-TCR_{1045} T cells expressing different congenic markers to facilitate tracking each population of the engineered T cells over time in the same treated host within the same TME (Fig. 6 G). We found that, 10 d after infusion, ACADVL-TCR_{1045} T cells were present in the tumor at significantly higher numbers than TCR_{1045} T cells (Fig. 6 H), showing a better T cell metabolic fitness and survival advantage. This preferential survival of ACADVL-TCR_{1045} T cells was even more pronounced at 21 d after infusion, suggesting that T cells expressing *ACADVL* have improved survival and persistence in a metabolically hostile TME. ACADVL-TCR_{1045} T cells were also found in greater numbers in the spleen and blood relative to TCR_{1045} T cells (Fig. S4 D), suggesting that expression of *ACADVL* may confer an overall survival advantage to $CD8^+$ T cells.

TCR_{1045} T cells infiltrating the TME have been shown to already exhibit reduced ability to produce antitumor cytokines by day 8 and to then become progressively dysfunctional and express high levels of inhibitory receptors, consistent with an exhausted phenotype by day 28 after entering KPC tumors (Nieman et al., 2011; Stromnes et al., 2015). Therefore, we investigated whether ACADVL-TCR_{1045} T cells preferentially retained effector function in the TME. By 10 d after injection, ACADVL-TCR_{1045} T cells expressed only low levels of PD-1, Tim-3, Lag-3, and TIGIT (T cell immunoreceptor with Ig and ITIM domains; Fig. S4 E), similar to what was reported for $TCR_{1,045}$ T cells. Further, both T cell populations isolated from the tumor 10 d after transfer already produced reduced amounts of IFNγ and TNFα compared with their splenic counterparts, but similar amounts of cytokine relative to each other (Fig. S4 F).

Together, these data suggest that metabolic reprogramming of engineered TCR_{1045} T cells by increasing *ACADVL* expression can improve the persistence of effector $CD8^+$ T cells in the hostile TME, a substantive obstacle for $CD8^+$ T cells targeting solid tumors. However, *ACADVL* expression in $CD8^+$ T cells does not directly address the suppressive features of the PDA TME, and achieving sustained therapeutic benefit will likely require strategies not only to enhance metabolic fitness and survival, such as by increasing *ACADVL* expression, but also modulation of inhibitory pathways, such as by checkpoint blockade.

Human intrapancreatic $CD8^+$ T cells down-regulate ACADVL in the human lipid-rich TME

To assess the translational potential of our findings, we initially evaluated seven matched pairs of human PDA and adjacent normal tissues. Red Oil staining confirmed the tendency of human PDA tumors to accumulate neutral lipids (Fig. S5 A), and we then performed IMS to discern the compositional features of the human TME, as we had done above in the mouse studies. Similar to the murine model, we found that LC glycerophospholipids accumulated in five of the seven human PDA samples (Fig. 7 A), and that this accumulation was most apparent for PEs and PIs

(~10% increase, as highlighted by dotted lines in Fig. 7 B, and less for other classes; Fig. S5 B). As in murine samples, VLC sphingomyelins were by contrast relatively decreased (Fig. S5 B).

Motivated by these similarities with our murine model, we examined whether human CD8+ T cells also undergo transcriptional reprogramming and metabolic dysfunction when infiltrating the lipid-rich TME. Single-cell RNA-seq on 12 human PDA tumors and 9 matched adjacent normal pancreatic tissues confirmed that CD8+ T cells infiltrating these two different pancreatic microenvironments were transcriptionally distinct (Fig. 7 C and Fig. S5, C and D). In particular, human PDA-infiltrating CD8+ T cells had reduced expression of genes associated with a cytotoxic signature (Fig. 7 D) and transcriptionally resembled previously described exhausted T cells (Wherry et al., 2007; Fig. S5 F), as observed with the CD8+ T cells infiltrating the murine late PanINs. Of note, CD8+ T cells infiltrating PDA showed diminished expression of *ACADVL* (Fig. S5 E).

Multispectral image analysis of 22 samples of chronic pancreatitis and 96 PDA tumors probed with specific fluorescence-conjugated antibodies (Fig. 7 E) affirmed at the protein level the specific down-regulation of ACADVL in tumor-infiltrating CD8+ T cells (Fig. 7 F), demonstrating this to be a metabolic deficit that cytotoxic T cells acquire when infiltrating human PDA tumors. Altogether, these data reinforce a new model of tumor-specific T cells becoming metabolically dysfunctional in the TME of PDA and support future clinical studies of therapeutic modulation of ACADVL expression as a tool to increase metabolic fitness of tumor-specific T cells, and thus ultimately the efficacy of ACT.

Discussion

The initial hypothesis that the density of the desmoplastic pancreatic TME prevented the influx of T lymphocytes, has been weakened by the fact that CD4+ T cells are abundant within the tumor (De Monte et al., 2011; McAllister et al., 2014; Zhang et al., 2014). In agreement, we show here, in a genetically engineered tumor model, that an immune response is recruited to the PDA TME early during progression. However, such a response is significantly contracted in numbers and functionality at late time points, in part as a consequence of being subjected to a combination of immunosuppressive mechanisms. Among such mechanisms, blockade of the immune checkpoint (ICB) has unprecedented therapeutic impact on a subset of tumors, motivating increased efforts to target the interactions between immune cells and the TME. Despite data from us and others (Diana et al., 2016; Shen et al., 2017; Winograd et al., 2015) showing that inhibitory checkpoint molecules are up-regulated in CD8+ T cells infiltrating PDA, ICB has lacked clinical efficacy in pancreatic cancer (Brahmer et al., 2012), suggesting that additional mechanisms account for the lack of response. Because the mediators of immune surveillance are metabolically interconnected in the TME with tumor cells, including competing for the same nutrients (Kishton et al., 2017), a deeper understanding of the metabolic state of the PDA TME may offer essential insights into the obstacles to PDA immunity and suggest complementary approaches to improve the efficacy of immunotherapy of PDA, including ICB.

Along with a limited availability of extracellular glucose and the decrease of glycolytic hexose intermediates, our time- and space-resolved compositional analysis of the PDA TME suggested that CD8+ impairment could be further rooted in metabolic dysfunction (Chang et al., 2015; Ho et al., 2015; Sukumar et al., 2015). Indeed, when glycolysis is limited, CD8+ T cells should have the metabolic flexibility to switch to mitochondrial OXPHOS (Chang et al., 2015; Sena et al., 2013), as a means to maximize the production of energy and reducing equivalents necessary to exert their effector functions (Zhang et al., 2017). This might be particularly useful for CD8+ T cells infiltrating the PDA TME, in which the low availability of glucose is paralleled by accumulation of VLCFAs. However, whereas tumor cells evolved to survive by feeding their bioenergetic needs with FAO (Vander Heiden et al., 2009), our study reveals that the transcriptional reprogramming experienced by intrapancreatic CD8+ T cells interferes with their ability to metabolize LCFAs, further contributing to their exhaustion. In this context, our data pinpoint ACADVL down-regulation as a crucial event. Indeed, impaired VLCAD enzymatic activity elicited accumulation of specific LC lipids, pronounced mitochondrial insufficiency, and failure of the effector functions. Remarkably, this closely recapitulates symptoms and biochemical findings in patients who inherited VLCAD deficiency. Indeed, situations of increased energy demand may induce lethargy, hypoketotic hypoglycemia, coma, and death, especially during fasting, viral illnesses, and prolonged physical exercise, because of a severe energy deficiency and the accumulations of toxic acylcarnitines (Wanders et al., 1999; Spiekerkoetter et al., 2003).

In addition to undermining their energy supply, this metabolic defect may subvert some of the biosynthetic pathways that govern CD8+ T cell effector functions, at both structural and signaling levels. For example, cholesterol and glycosphingolipids form signaling hubs in the plasma membranes of T cells known as lipid rafts that are essential for immune cell activation and function (Jury et al., 2007; Lingwood and Simons, 2010; Yang et al., 2016). Changes in the lipid composition affect the biophysical properties of lipid rafts (Janes et al., 2000) and, consequently, influence TCR signaling and contribute to defining functional T cell phenotypes (Köberlin et al., 2015). Moreover, the metabolic reprogramming associated with immune cell activation relies on the mevalonate pathway that generates cholesterol, the ubiquinone necessary for the mitochondrial electron transport chain, and a series of other bioactive intermediates (Gruenbacher and Thurnher, 2017). Interestingly, the classes of lipids that we have found to be enriched in the TME have been suggested to play roles in PDA in cell signaling disruption (e.g., PIs; Martin, 2003) and lipid raft formation (e.g., sphingolipids; Murai, 2012). When combined with the lipidomic analysis, our longitudinal IMS profiling suggests that the enrichment of some glycerophospholipids containing LC and VLC in the TME (starting in early PanINs in a context poor in glucose) temporally coincides with LC lipid uptake while preceding the accumulation of FAs (preferentially LC) and prenol lipids (a product of mevalonate pathway) and the appearance of the metabolically exhausted phenotype in intratumor CD8+ T cells. A possible explanation could impute the transcriptional

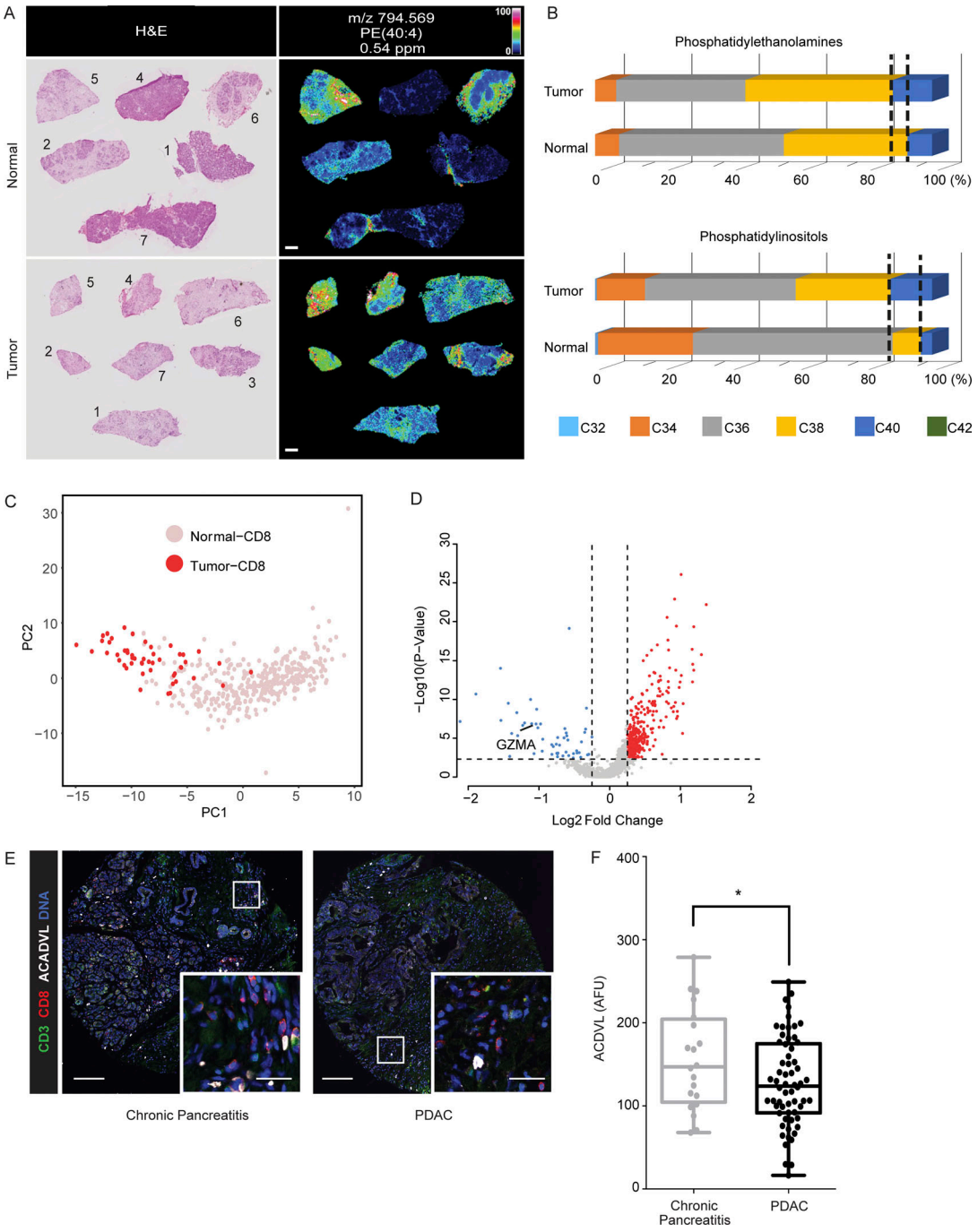

Figure 7. **Lipid accumulation and ACADVL dysfunction in human CD8⁺ T cells infiltrating PDA. (A)** H&E staining (left panel) and intensity distribution of a representative m/z species by IMS (right panel) in seven matched human PDA (T) and normal adjacent tissue (N). N tissue from patient 3 was not available. Scale bar = 2 mm. **(B)** Bar plots showing the relative fraction of lipids of various FA chain length detected at the different disease time points for PE (upper) and PI (lower) lipids (FAs for the two lipid types were summed). **(C)** First two principal components of the transcriptome of intrapancreatic CD8⁺ T cells from human PDA samples (dark red, *n* = 4) and adjacent normal tissues (light red, *n* = 4). **(D)** Volcano plot of differentially expressed genes in human PDA samples (dark red, *n* = 4) and adjacent normal tissues (light red, *n* = 4); P < 0.005. **(E and F)** Representative imaging (E) of immunofluorescence staining of pancreatic disease spectrum tissue array using fluorophore-conjugated specific antibodies targeting human CD8 (red), CD3 (green), and ACADVL (white). Nuclei were stained with DAPI (blue). The TMA included 84 cores of PDA and 44 of chronic pancreatitis. Scale bar = 100 µm; insets = 50 µm. **(F)** Quantification of ACADVL expression as absolute fluorescence unit (AFU) in segmented human CD8⁺ T cells infiltrating PDA versus chronic pancreatitis. Egrror bars represent mean ± SEM. Statistics were calculated using unpaired Student's *t* test; *, P ≤ 0.05–0.01.

reprogramming to the progressive intracellular accumulation of lipids as an attempt to reestablish lipid homeostasis and limit lipotoxicity. Our data support this model, for example by showing reduced expression in $CD8^+$ cell from late PanINs of sterol regulatory element binding transcription factor 1 (*SREBF1*), which governs the expression of enzymes belonging to the mevalonate pathway, namely *MVD* and *IDI1* genes, and FAO, in particular *ACADVL*. Mechanistically, the transcriptional reprogramming, which includes ACADVL down-regulation, could result from the prolonged cellular stress induced by lipid accumulation (Fu et al., 2011; Shao and Espenshade, 2012), as indicated by up-regulation of key genes involved in peroxisome biogenesis (Lodhi and Semenkovich, 2014) and ER stress, overall down-regulation of the unfolded protein response (UPR) pathway (Fig. S3 B), and dysfunctional mitochondria (Aon and Camara, 2015). Thus, low VLCAD enzymatic activity could amplify specifically the accumulation of LCFAs, worsening their associated toxicity. Indeed, the initial increase in intracellular lipids might be tolerated by increasing the conversion of diacylglycerol into triacylglycerol species, with their subsequent deposition between the ER membranes and the generation of LDs (Hapala et al., 2011). However, chronic exposure to LCFAs such as palmitate precludes LD formation, increases ER stress, dampens the UPR mechanism, and impacts the activity of mitochondria, in particular at the level of the mitochondria-associated ER membrane (Shinjo et al., 2017), where proteins like VDAC3 (Fig. 5 B) seem to play an important role (Messina et al., 2014). The early appearance of LDs in intrapancreatic $CD8^+$ T cells and their decrease coinciding with the dysfunctional state of $CD8^+$ T cells further supports this model (Gao and Goodman, 2015; Kim et al., 2016; Vevea et al., 2015), suggesting that changes in the TME may drive the transcriptional responses in infiltrating $CD8^+$ T cells and, ultimately, lead to their metabolic exhaustion.

A question that warrants further study is why these metabolic defects are peculiar to $CD8^+$ T cells. In our experiments, we found that $CD4^+$ T cells and myeloid $CD45^+$ $CD3^-$ cells adapt to the lipid-rich PDA TME, becoming able to tolerate the increased uptake of LC lipid uptake and still preserving mitochondrial function. In particular, the up-regulation of VLCAD might confer a metabolic advantage to $CD4^+$ T cells, the majority of which are likely T reg cells (Carstens et al., 2017; Hwang et al., 2016; Jang et al., 2017; Protti and De Monte, 2013). Indeed, it is known that the TME favors their survival while limiting $CD8^+$ T cell activation, and this difference may reflect the ability of T reg cells to engage glycolysis, FA synthesis, and oxidation (Berod et al., 2014; Pacella et al., 2018; Procaccini et al., 2016). In agreement, data from us and others show that T reg cells increase in the pancreas during PDA progression (Fig. 2 B). Previous studies have demonstrated that $CD4^+$ T reg cells are reprogrammed by FoxP3 to function in low-glucose environments (Angelin et al., 2017; Howie et al., 2017). Thus, $CD8^+$ T cells, compared with other immune infiltrating cells, do not appear to have the necessary metabolic flexibility to survive in the hostile TME.

Our study paves the way for improving the efficacy of immunotherapy based on insights from the metabolic characterization of the TME. For instance, both $CD4^+$ T cells (Fig. 5 E) and PDA tumor cells (Bailey et al., 2016) adapt to the lipid-rich TME by up-regulating VLCAD. Based on our data, systemic interventions aiming to inhibit FAO in tumors (Molina et al., 2018) or to activate it in immune cells (Scharping et al., 2016; Zhang et al., 2017) should be carefully weighed, because of the detrimental impact they could have on the $CD8^+$ T cell survival and persistence. ATCs with engineered T cells is being evaluated for the treatment of PDA, with pioneering works in mice (Stromnes et al., 2015) and humans (Beatty and Moon, 2014) demonstrating feasibility, safety, and ability to mount therapeutic responses against pancreatic tumors. However, these T cells undergo a progressive loss of function and persist poorly, ultimately failing to maintain long-term activity and tumor eradication. Limited infiltration of infused tumor-reactive T cells, loss of function in cells that do infiltrate, and the inability to survive in the TME are substantive obstacles for ATC against solid tumors. Combining metabolic reprogramming to confer better metabolic fitness, engineered tumor-specific T cells may address some of these issues. Our data demonstrate that enhancing *ACADVL* expression improves the ability to respond to metabolic stress and, consequently, improves the ability of the T cells to persist and survive even in a metabolically unfavorable environment. Nevertheless, metabolic reprogramming has only a marginal effect on T cell function or the expression of inhibitory receptors. Thus, successful ATC will likely benefit from not only metabolically reprogramming T cells but also directly enhancing function, such as by combining with checkpoint blockade.

Although the first descriptions of fatty infiltration in the pancreas or fatty replacement in pancreas cells dates back nearly a century (Ogilvie, 1933; Schaefer, 1926), the origin of the fatty deposits and prognostic impact of such findings on the development and progression of pancreatic tumors has not been determined. Risk factors for pancreatic cancer such as obesity and metabolic syndrome are associated with increased circulating free FAs, which could infiltrate and accumulate in the pancreas, particularly after the death or damage of normal acinar pancreatic tissue (Smits and van Geenen, 2011). Pancreatic steatosis closely recapitulates the course of nonalcoholic fatty liver disease, with accumulated fat generating high levels of oxidative stress and consequent release of proinflammatory cytokines (Lesmana et al., 2015). Despite being often perceived as a benign condition, fat infiltrates are associated with tumor progression in PDA (Hori et al., 2014; Takahashi et al., 2018; Tomita et al., 2014), as well as other solid tumors such as prostate cancer (Chen et al., 2018; Nieman et al., 2011). Such findings further highlight the importance of characterizing, using the approaches described here, the nature of lipid deposits identified not only in PDA but in other cancer types.

Materials and methods

Animal studies

All animal studies and procedures were approved by the Institutional Animal Care and Use Committees in compliance with the *Guide for the Care and Use of Laboratory Animals*. Animals were housed in a pathogen-free facility on a 12-h light/dark cycle and received food (standard rodent chow) and water ad libitum.

All manipulations were performed under Institutional Animal Care and Use Committee–approved protocols. The KC (p48Cre; LSL-Kras^{G12D}) and KPC (p48Cre; *Tp53*$^{LSL\text{-}R172H}$;LSL-Kras^{G12D}) mouse models have been described (Hingorani et al., 2003, 2005). The mice were housed at MD Anderson Cancer Center (Houston, TX) and Fred Hutchinson Cancer Research Center (Seattle, WA).

Histology and immunohistochemistry

Tissues were fixed in 10% formalin and embedded in paraffin. Sections (4 µm) were stained with H&E. Slides were scanned, and images were captured with a Nikon DS-Fi1 digital camera using a wide-field Nikon EclipseCi microscope and analyzed in blind by our pathologist, who scored the pancreatic sections as early and late PanIN lesions.

Immunofluorescence

Tissues were fixed in 4% formaldehyde for 24 h at room temperature, moved into 70% ethanol for 12 h, and then embedded in paraffin (Leica, ASP300S). After cutting (Leica, RM2235) and baking at 60°C for 20 min for deparaffinization, slides were treated with citric acid–based antigen unmasking solution (Dako) for antigen retrieval according to the manufacturer's instructions. Nonspecific signals were blocked using 5% goat serum for 1 h, and samples were stained overnight with primary antibodies at 4°C. Slides were incubated with species-specific secondary Alexa-conjugated antibodies (Invitrogen, 1:1,000) and mounted with Prolong Gold anti-fade plus DAPI (Life Technologies). Images were captured with a Nikon high-speed multiphoton confocal microscope (A1 R MP). Quantification was performed blinded by counting labeled cells in three to five high-power fields (40×) from three to eight mice per group. Primary antibodies used included CD3, CD4, CD8a, aSMA, e-cadherin, and ACADVL.

For quantification of neutral lipid by confocal microscopy, pancreatic tissue sections labeled with DAPI, Alexa Fluor 647–conjugated anti-CK19 antibody (Abcam), anti-CD8a primary antibody, Alexa Fluor 488–conjugated anti-rat secondary antibody, and LipidTOX Red (Thermo Fisher Scientific), were imaged on a Leica SP8 (Leica Microsystems) with a 25×/0.95 water-immersion objective lens. Z-stacks of the whole sections were acquired with Leica Navigator software, voxel size 0.3 × 0.3 × 1.5 µm in x, y, and z. The quantification of T cells in tissue and LDs in tissue and tumor areas was done on the maximum projections with a homemade ImageJ (National Institutes of Health) macro. Briefly, the tissue area was segmented according to the tissue autofluorescence in the green channel. The tumor areas were identified and segmented according to the e-cadherin staining, and the LDs were segmented according to the specific fluorescent red signal. The number of LDs and the LD area were calculated in the whole tissue and the tumor, and the T cells were identified and counted according to the specific Alexa Fluor 488 signal by the ImageJ macro. The automatically identified T cells were visually checked in the images, and the total T cell number was eventually corrected. In each T cell, the presence of LDs was evaluated by analyzing the original Z-stack to confirm the occurrence of LDs inside the cell cytoplasm. For each sample, a tissue area of ≥2 mm^2 was analyzed.

Isolation of T cells from tissues

T cells were harvested from spleens and pancreatic samples. Briefly, single-cell suspensions were generated by mincing spleens with mesh screens in TCM medium followed by passing cells through a 40-µm filter (Thermo Fisher Scientific). Red blood cells were lysed with 1× RBC lysis buffer (eBioscience). To obtain tumor-infiltrating lymphocytes, tumors were harvested, cut into small fragments, and treated with 0.8 mg/ml collagenase IV and trypsin inhibitor (Sigma-Alrich) in HBSS 1× (Thermo Fisher Scientific) for 20 min at 37°C. Tumor fragments were homogenized, washed, and strained through a 70-µm filter.

T cell culture with FAs

CD8$^+$ T cells freshly isolated from spleens of C57BL6 mice by flow cytometry cell sorting were incubated in complete medium supplemented with Palm (Agilent), Lino (Sigma-Aldrich), or a mixture of Palm and BSA-Oleate (Sigma-Aldrich) used at 100-µM concentration.

TEM

TEM was performed at the University of Texas MD Anderson Cancer Center High-Resolution Electron Microscopy Facility. CD8$^+$ and CD4$^+$ T cells were sorted from spleens and pancreata of mice bearing early and late PanIN lesions. Samples were fixed with a solution containing 3% glutaraldehyde plus 2% paraformaldehyde in 0.1 M cacodylate buffer, pH 7.3, for 1 h. After fixation, the samples were washed and treated with 0.1% Millipore-filtered cacodylate-buffered tannic acid, postfixed with 1% buffered osmium tetroxide for 30 min, and stained en bloc with 1% Millipore-filtered uranyl acetate. The samples were dehydrated in increasing concentrations of ethanol, infiltrated, and embedded in LX-112 medium. The samples were polymerized at 60°C for 2 d. Ultrathin sections were cut using a Leica EM FC7 ultramicrotome. After contrasting with uranyl acetate and lead citrate, sections were analyzed with a Leo 912AB transmission electron microscope (Carl Zeiss). Images were acquired with a 2K bottom-mounted slow-scan Proscan camera controlled by EsivisionPro 3.2 software. For morphometrical analysis, for each experimental condition, 25 random whole cellular profiles were acquired by stitching together several images acquired at a nominal magnification of 6,300× (pixel size, 1.77 nm). Using ImageJ, mitochondria present in each cellular profile were classified as normal (narrow and long cristae with uniform and moderate electron-dense matrix), swollen (with increased size and patchy electrolucent matrix), or hypercondensed (very electron-dense matrix with dilated cristae). The few mitochondria for which the assignment to one category was not possible (less than optimal ultrastructural preservation or an unfavorable plane of section) were not considered in the analysis.

Lipid staining

Histologic visualization of fat cells and neutral fat was performed using the Oil Red O Kit from Abcam. Briefly, frozen mouse or human pancreatic sections were placed in propylene glycol for 2 min and incubated with Oil Red O Solution. Sections were differentiated in a mixture of 85% propylene glycol in

distilled water, stained with hematoxylin, and mounted with aqueous mounting medium.

Glucose assay

Glucose concentrations in pancreas supernatant from early and late PanINs were measured using the Glucose Assay Kit (Eton Bioscience). For ex vivo glucose levels, harvested samples were weighed and minced in fixed amounts of PBS. Glucose concentration was quantified relative to the weight of tumors and the volume of collected supernatant, and normalized with glucose concentrations in WT tumors.

Seahorse extracellular flux analysis

Seahorse experiments were performed on sorted intrapancreatic $CD8^+$ and $CD4^+$ cells using XF Cell Mito Stress kit (Seahorse Bioscience). OCR and ECAR were measured with XF96 Extracellular Flux Analyzers (Seahorse Bioscience) as previously described (van der Windt et al., 2016). Briefly, cells were plated on poly-D-lysine–coated 96-well polystyrene Seahorse plates (100,000 T cells/well), equilibrated for 1 h at 37°C, and assayed for OCR (pmol/min) and ECAR (mpH/min) in basal conditions and after addition of oligomycin (1 µM), carbonyl cyanide-4-phenylhydrazone (1.5 µM), and antimycin A/rotenone (1 µM/0.1 µM).

Flow cytometry and cell sorting

Fluorophore-conjugated antibodies were purchased from BD Biosciences: CD45 (30-F11), CD3 (145-2C11), CD8α (53-6.7), CD4 (GK1.5), Thy1.1 (OX-7), Thy1.2 (53–2.1), CD69 (H1.2F3), CD44 (IM7), PD1 (29F.1A12), Lag3 (C9B7W), Tim3 (RMT3-23), TIGIT (1G9), 4-1BB (17B5), and Vb9 (MR10-2). Reagents were obtained from BD Bioscience, eBioscience, and BioLegend. The $MSLN_{406–414}$/H-2Db tetramer was conjugated to APC by the Fred Hutchinson Immune Monitoring Core. Msln peptides were purchased from Elim Peptide. For intracellular cytokine production, 10^6 cells isolated from spleen or primary tumors were incubated for 5 h in Golgiplug (BD Biosciences) with or without $MSLN_{406–414}$ peptide, stained for surface markers, fixed with BD Biosciences Fix/Perm, permeabilized using BD Biosciences Perm/Wash, and incubated with antibodies to IFNγ (XMG1.2), TNFα (MP6-XT22), IL-2 (JES6-5H4), and Granzyme B (GB11). For transcription factor staining, Tbet (4B10) and Eomes (Ef450) were purchased from BD, and cells were stained for surface markers, fixed with the eBioscience Fix/Perm kit, permeabilized using eBioscience Perm/Wash Buffer, and stained intracellularly. Cell sorting was performed using a FACSAria II (BD) with >95% purity based on the exclusion of dead cells and the expression of CD45, CD3, and CD4/CD8. For mitochondrial studies, cells were incubated with 50 nM MitoTracker Green and/or 25 nM MitoTracker Orange for 30 min at 37°C before staining. Reagents were obtained from Life Technologies. All panels were stained with LIVE/DEAD fixable Aqua stain or Ghost Dyes from TONBO before surface or intracellular staining. UltraComp eBeads were used for all compensation. All FACS data were acquired using a BD-LRSFortessa X-20 and analyzed with FlowJo software.

Bodipy and 2-NBDG in vivo treatment

Mice were injected i.p. with 50 µg Bodipy FL C16 (Thermo Fisher Scientific) in 50 µl DMSO or with 100 µg 2-NBDG (Cayman Chemicals) in PBS, 60 or 20 min, respectively, before sacrifice and cell isolation.

Lipidomic analysis on T cells

Liquid chromatography–MS lipidomic analyses were performed on sorted intrapancreatic T cells using reverse-phase liquid chromatography (RPLC) coupled with positive- and negative-mode electrospray-ionization high-resolution MS. Lipids from the samples were extracted using the Folch extraction method. Briefly, cell pellets were resuspended in 100 µl ammonium formate buffer, 50 mM, pH 6.8, followed by the addition of 400 µl ice-cold methanol. Each sample was vortexed and sonicated for 10 pulses at 30% power using a sonication probe while cooling on ice. 800 µl chloroform and 100 µl water were added to each sample to a final ratio of 4:2:1 chloroform:methanol:water. Samples were vortexed, incubated on ice for 10 min, and spun down at 1,000 rpm for 10 min. The bottom layer (organic layer containing the lipids) was transferred to a clean Eppendorf tube, and the extraction with chloroform of the aqueous layer was repeated once. The organic layers (lipid layers) were coupled and dried down under vacuum. Before MS analysis, dried lipids were reconstituted in chloroform:methanol (50:50, vol/vol) containing an internal heavy labeled lipid standard (Splash Lipidomix Mass Spec Standard; Avanti Polar Lipids) and centrifuged for 5 min at 15,000 rpm to remove insoluble material. Samples were volume adjusted to ensure that cell count per volume (µl) was normalized. Global untargeted lipidomic analyses were performed using full MS and data-dependent acquisition analyses on a Q-Exactive HF hybrid quadrupole-Orbitrap mass spectrometer (Thermo Fisher Scientific) equipped with a Vanquish UHPLC binary system and auto-sampler (Thermo Fisher Scientific). Extracts (5-µl injection volume for RPLC-POS and 6 µl for RPLC-NEG) were separated by RPLC on a Hypersil Gold 1.9-µm, 2.1 × 100-mm column (Thermo Fisher Scientific) held at 40°C. Reverse-phase separation was performed at 250 µl/min using solvent A (0.1% formic acid in water) and solvent B (0.1% formic acid in isopropanol:acetonitrile:water [60:36:4]) with the following gradient: 30% B for 0.5 min, 30–70% B over 1.5 min, 70–99% B over 13 min, 99–10% B over 1 min, 10% B held 4 min, 10–30% B over 1 min, and 30% B held over 5 min (gradient length 30 min).

Ultra-performance liquid chromatography/tandem MS raw data were imported, processed, normalized, and reviewed using Progenesis QI v.2.1 (Non-linear Dynamics). All sample runs were aligned against a quality control pool reference run, and peak picking was performed on individual aligned runs to create an aggregate dataset. Features (retention time and m/z pairs) were combined using both adduct and isotope deconvolution. Data were normalized to the spike-in lipid standards as an abundance ratio. Statistically significant changes were identified using multivariate statistical analysis, including PCA, and P values were generated using ANOVA or pairwise comparison. Tentative annotations (Schrimpe-Rutledge et al., 2016) were made within Progenesis using accurate mass measurements (<5 ppm error), isotope distribution similarity, and assessment of fragmentation spectrum matching (when applicable) from the Lipid Maps database (Fahy et al., 2007). Four biological replicates and

two technical replicates from each sample type were used to calculate the fold change and P value, and features were considered differentially expressed only if they met both criteria of fold change ≥|2| and significance ($P \leq 0.05$). Heatmap visualization of individual lipid features was performed using Metaboanalyst 4.0 software (Chong et al., 2018) using Pearson average clustering algorithm. To assess instrument performance and reproducibility throughout our experimental run sequence, the retention times and peak areas of SPLASH Lipidomix standards were monitored.

Human specimens

All studies using human specimens were approved by the University of Texas MD Anderson Cancer Review Board. Tumor tissues were obtained from patients who provided written informed consent for collection and analysis of tumor samples under Institutional Review Board–approved protocols. Informed consent was obtained from each patient before tumor tissue collection. To ensure patient confidentiality, no information on age, sex, or ethnicity was provided to the investigators of this study.

RNA-seq and gene expression analysis

$CD8^+$ T cells were sorted with >95% purity using FACSAria from BD directly into RLT lysis buffer (Qiagen). RNA was isolated from purified cells using RNeasy Mini kits (Qiagen), and RNA concentrations were determined using Nanodrop. Fastqc software was used on the fastq files to generate the quality control report, and Tophat software was used to align the sequences to the mouse genome mm10. HTSeq was used to count the read number of genes from each sample. Genes with read counts <10 in all the samples were considered to be noise and therefore removed. The obtained read counts are analogous to the expression level of each gene across all the samples. Differential expression analysis were performed using DESeq2 (Love et al., 2014). Genes with raw mean reads >10 (i.e., ∼9,225 genes) were used for normalization and differential gene expression analysis using DESeq2 package in R. The Wald test defined in the DESeq function of the package was used for differential expression and further downstream analysis. PCA, hierarchical clustering plots (hclust), and XY plots between replicates of the same genotypes were used to examine for nominal amounts of nontechnical variation and other latent factors. PCA and volcano plots were generated using ggplot2 package, and all the heatmaps were generated using pheatmap or heatmap2 package in R environment. Gene overlap analysis was performed against the Molecular Signatures Database (Liberzon et al., 2015; Subramanian et al., 2005) Investigate Gene Sets web program under GSEA.

RT^2 Profiler PCR arrays

Gene expression analysis of 84 key genes involved in FA metabolism was assessed on naive or in vitro–activated $CD8^+$ T cells using a Mouse Fatty Acid Metabolism RT^2 Profiler PCR Array (Qiagen; PAMM-007Z) according to manufacturer instructions. Ct values were exported to an Excel file for data analysis using the provided web tools (http://www.qiagen.com/geneglobe). Ct values were normalized based on a panel of reference genes. The data analysis web portal calculates fold changes using using the ΔΔCt method followed by ΔΔCt calculation ($\Delta Ct_{test\ group} - \Delta Ct_{control\ group}$). Fold change is then calculated using $2^{(-\Delta\Delta Ct)}$ formula. Data were plotted using scatter plot and heatmap.

Imaging MS

Frozen pancreata were sectioned at 10 µm on a CM3050S Cryostat (Leica Biosystems; chuck temperature of −20°C, chamber temperature of −24°C). Serial sections were alternately thaw mounted onto microscope slides (Thermo Fisher Scientific) for histology and onto a gold-coated stainless-steel target for IMS and stored at −80°C until use.

Gold-coated targets with tissue sections were removed from the freezer and allowed to warm to room temperature in a vacuum desiccator to prevent water condensation on the slide. 2,5-dihydroxyacetophenone (Sigma-Aldrich) was used as a MALDI matrix in both positive and negative ion modes and was applied to the slide using a custom-built sublimation apparatus (110°C, <70 mtorr, 6.5 min), as previously described (Hankin et al., 2007). Slides for histologic analysis were stained with H&E and analyzed using a SCN400 Brightfield Slide Scanner (Leica Microsystems) or analyzed by immunofluorescence.

MALDI IMS was performed on either a 15T or 9.4T SolariX FT-ICR mass spectrometer (Bruker Daltonics) equipped with an Apollo dual MALDI/ESI source. The MALDI source uses a Smartbeam II 2 kHz Nd:YAG (355-nm) laser that has been modified to provide a Gaussian beam laser profile. Positive-ion-mode mouse pancreas lipid images were acquired from m/z 500 to 2,000 on the 15T FT-ICR MS using a time-domain file size of 512K, resulting in an ICR transient length of 0.5767 and a resolving power of ∼100,000 at m/z 796.525. An internal lock mass calibration (m/z 734.5694, $[PC(32:0)+H]^+$) was used during image acquisition, and a multipoint external mass calibration was performed after data acquisition using common PC ions generated from the tissue samples. Images were acquired using a 75-µm raster step and 400 shots per pixel. Negative-ion-mode mouse pancreas lipid images were also acquired from m/z 500 to 2,000 on the 15T FT-ICR MS using a time-domain file size of 512K. An internal lock mass calibration (m/z 885.5494, $[PI(38:4)-H]^-$) was used during image acquisition, and a multipoint external mass calibration was performed after data acquisition using common glycerophospholipid ions generated from the tissue samples. Images were acquired using a 75-µm raster step and 400 shots per pixel. Negative-ion-mode mouse pancreas metabolite images were acquired from m/z 100 to 1,400 on the 9.4T FT-ICR MS using a time-domain file size of 2M, resulting in an ICR transient length of 0.7340 and a resolving power of ∼215,000 at m/z 259.023. Images were acquired using a 100-µm raster step and 500 shots per pixel. Positive-ion-mode human pancreas lipid images were acquired from m/z 500 to 3,000 on the 9.4T FT-ICR MS using a time-domain file size of 256K, resulting in an ICR transient length of 0.4544 and a resolving power of 40,000 at m/z 796.525 An internal lock mass calibration (m/z 734.5694, $[PC(32:0)+H]^+$) was used during image acquisition, and a multipoint external mass calibration was performed after data acquisition using common PC ions generated from the tissue samples. Images were acquired using a

50-µm raster step and 500 shots per pixel. Negative-ion-mode human pancreas lipid images were acquired from m/z 500 to 2,000 on the 9.4T FT-ICR MS using a time-domain file size of 256K. An internal lock mass calibration (m/z 885.5494, [PI(38:4)-H]) was used during image acquisition, and a multipoint external mass calibration was performed after data acquisition using common glycerophospholipid ions generated from the tissue samples. Images were acquired using a 50-µm raster step and 500 shots per pixel. All ion images were generated using FlexImaging 5.0 (Bruker Daltonics) and plotted as ±0.005 daltons using root mean square normalization unless otherwise noted.

Lipids were identified using accurate mass measurements (<5 ppm) by searching against the LIPID MAPS (Lipidomics Gateway, http://www.lipidmaps.org) and METLIN (The Scripps Research Institute, https://metlin.scripps.edu) online databases and are reported using total carbon: double bond nomenclature. Lipid identification data analysis was performed using DataAnalysis and Compass IsotopePattern (Bruker Daltonics) as well as the mMass software package (Strohalm et al., 2008).

To visualize the global lipidomic changes in IMS data across multiple time points, a novel data analysis strategy was developed using both SCiLS (Bruker Daltonics) and R. SCiLS bisecting *k*-means clustering was used to segment regions of interest in the root mean square–normalized imaging data that positively correlated with CD8 immunostaining performed on serial tissue sections. Early-stage (9 and 13 wk) and late-stage (20 and 30 wk) IMS data were pooled and compared with a control (4 wk). An in-house-written R program that uses the LIPID MAPS database was used to extract the mean intensity values for each accurate mass lipid identification ±0.0009%. The resulting list was exported from SCiLS as a .csv file and imported into R. A second in-house-written R script was used to filter this list and generate a heatmap of log2 fold change intensity values. The filters in the program were used to reduce false-positive results as well as remove lipids with zero intensity in the control group, log2 values between 1 and −1, and intensity values <0.5 of the quantile in the control group. The lipids in the heatmap were sorted by head group, fatty acyl chain length, and level of fatty acyl chain unsaturation. These exported data were also used to make the horizontal bar plots. Briefly, the m/z peak list was searched against the LIPID MAPS database. Isotopic distributions of identified lipids were confirmed manually before importing a list of the lipid identifications and mean intensity values into Excel. Intensities of lipids with different levels of fatty acyl chain unsaturation but the same total fatty acyl chain length were summed within each separate lipid class (e.g., the intensities of PC(34:2) and PC(34:1) were summed). Within each lipid class, the intensity of each total fatty acyl chain length group was normalized to the total intensity of all ions within the lipid class so as to readily compare changes in the relative lipid compositions at multiple time points. For these bar plots, PI(38:4) was removed from the analyses for both sets of samples because it is extremely abundant and distorted the bar plots. The PCs and sphingomyelins were detected in positive ion mode, and the relative intensities reflect the summed distributions of the $[M+H]^+$, $[M+Na]^+$, and $[M+K]^+$ ion types. Ether and vinyl ether (plasmalogen) lipids as well as modified (e.g., by lipid peroxidation) lipids were excluded from the bar plot analyses. IMS quantification was performed by exporting the pixel intensities of the pooled data segments and removing zero-intensity values (attributed to peak picking inaccuracy). These data were used to calculate the average and SEM for this replicate, reflecting the heterogeneity of the disease at each stage.

TCR transduction of murine T cells

The ecotropic retroviral packaging cell line, Platinum (Plat)-E cells (Cell Biolabs), were plated (2.2×10^6 cells) in PLAT-E medium (DMEM, 10% FBS, 10 µg/ml blasticidin, 1 µg/ml puromycin, and 100 U/ml penicillin/streptomycin) on 10-mm culture plates. After 24 h, Plat-E cells were transfected with DNA encoding the desired TCR and/or construct using the Effectene transfection kit (Qiagen). At 48 h, medium was replaced with T cell medium (IMDM, 10% FBS, 2 µM L-glutamine, 100 U/ml penicillin/streptomycin, and 25 µM 2-β-mercaptoethanol). On days 2 and 3 after transfection (at 72 and 96 h), virus-containing supernatant was collected. Splenic T cells isolated from P14 Thy1.1$^+$ mice were stimulated with α-CD3e (clone 145-2C11) and α-CD28 (clone 37.51; both from BD PharMingen) and IL-2 (50 IU/ml aldesleukin; University of Washington Pharmacy) and transduced with retroviral supernatant by spinfection in polybrene (5 µg/ml, 90 min at 1000 *g*) 24 and 48 h after T cell activation.

Adoptive immunotherapy

For T cell enrichment experiments, live CD8$^+$ Vβ9$^+$ T cells were sorted, mixed at a 1:1 ratio, and transferred into KPC tumor-bearing mice. Recipient mice received ≤10^7 total engineered T cells (stimulated once), cotransferred in equal numbers. For T cell phenotyping and function experiments, cells were sorted as above and cotransferred with ≤5×10^7 antigen-pulsed irradiated splenocytes followed by IL-2 (2×10^4 IU, s.c.) daily for 10 d to promote T cell expansion and survival. In all experiments, mice were treated with one dose of cyclophosphamide (180 mg/kg) i.p. ∼8 h before T cell transfer.

Ultrasound imaging

KPC mice underwent serial high-resolution ultrasound imaging (Vevo 2100) at 8 wk of age to monitor autochthonous tumor development. Mice were enrolled based on defined pancreatic mass with ≥3-mm diameter.

Single-cell RNA-seq on human samples

Single-cell transcriptome sequencing was performed on human PDA samples on the 10X Genomics Chromium platform using the Single Cell 3′ v2 chemistry per the recommended protocol. Data were processed using Seurat v2.2 in accordance with the recommended analysis for multisample data. All cells were clustered using sharing nearest neighbor, and the clusters most highly expressing CD3 genes were considered T cells and extracted for further analysis. T cells were then classified as CD4 or CD8 based on imputed expression of CD4 and CD8a/CD8b, respectively. Differential gene expression was performed using a Wilcoxon test with Bonferroni P value correction for multiple comparisons.

Data availability

Data are deposited in the Gene Expression Omnibus database under accession no. GSE147465.

Quantification and statistical analysis

All statistical analyses were conducted using GraphPad Prism 6. Differences between two groups were calculated by unpaired, two-tailed Student's *t* test. Multiple comparisons were performed by one-way ANOVA followed by Bonferroni's multiple comparison tests. Significance was set at P values ≤ 0.05. For all figures: *, P ≤ 0.05–0.01; **, P ≤ 0.01–0.001; ***, P ≤ 0.001–0.0001; ****, P ≤ 0.0001. Unless noted in the figure legend, all data are shown as mean ± SEM. The n numbers for each experiment and the numbers of experiments are noted in the figure legends.

Online supplemental material

Fig. S1 shows lipid accumulation and glucose and H6P decrease in TME during PDA progression. Fig. S2 shows $CD8^+$ T cells accumulating specific LC lipids and becoming dysfunctional during PDA progression. Fig. S3 shows transcriptomic analysis of $CD8^+$ T cells in vivo and in vitro. Fig. S4 shows how ACADVL overexpression confers enhanced metabolic fitness. Fig. S5 shows lipid accumulation and ACADVL deregulation in human $CD8^+$ T cells infiltrating PDA.

Acknowledgments

L. Nezi and T. Manzo dedicate this work to Leonardo and Lara Nezi. We thank V. Gopalakrishnan and A. Reuben for reagents; Liam McDonnel for thoughtful discussion; J. Wang and W. Ma for support with RNA-seq experiments; Kenneth Dunner Jr. for helping with electron microscopy experiments; and Caterina Bartolacci for preliminary lipidomic analysis. The lipidomic analyses were provided by the Vanderbilt University Center for Innovative Technology, Vanderbilt Institute of Chemical Biology; the Vanderbilt Institute for Integrative Biosystems Research and Education; and Vanderbilt University (S.D. Sherrod, G.S. Codreanu, and J.A. McLean).

This work was supported by the University of Texas MD Anderson Cancer Center Pancreatic Moon Shot to G. Draetta, Cancer Prevention and Research Institute of Texas grant RP160471 to G. Draetta, US Department of Defense grant W81XWH-11-1-0418 to G. Draetta, Associazione Italiana per la Ricerca sul Cancro StartUp grant to T. Manzo and core funding from IRCCS European Institute of Oncology to L. Nezi. IMS research was performed in the laboratory of R.M. Caprioli and supported in part by National Institutes of Health/National Institute of General Medical Sciences P41 GM103391-08 and National Institutes of Health/National Institute of Diabetes and Digestive and Kidney Diseases F32 FDK105841A (B.M. Prentic). Some of this research was performed at the MD Anderson Cancer Center Flow Cytometry and Cellular Imaging Facility, which is supported by National Cancer Institute grant P30CA016672. The work was also supported by National Cancer Institute grant CA33084 to P.D. Greenberg. This work was partially supported by the Ministero della Salute with Ricerca Corrente and 5x1000 funds.

Author contributions: T. Manzo and L. Nezi designed and coordinated the whole study. T. Manzo, K.G. Anderson, C.B. Nava Lauson, S. Tiberti, B.M. Bates, S. Tucci, and L. Nezi designed, executed, and analyzed experiments; B.M. Prentice, M.A. Jones, M. Reyzer, J.M. Spraggins, N.H. Patterson, and R.M. Caprioli designed and executed the IMS analysis; G.S. Codreanu, J.A. McLean, and S.D. Sherrod designed and executed the lipidomic analysis; A. Raman, A. Schalck, K. Rai, and N.E. Navin performed computational analysis; A. Raimondi and C. Tacchetti performed and analyzed TEM; J.A. Wargo and M. Kim obtained tissues from patients; S. Rodighiero and K. Clise-Dwyer analyzed experiments and provided technical assistance; T. Manzo, P.D. Greenberg, and L. Nezi analyzed the data, wrote, and edited the manuscript. Funding acquisition: T. Manzo, G. Draetta, and L. Nezi.

Disclosures: Dr. Manzo, Dr. Anderson, Dr. Bates, Dr. Greenberg, and Dr. Nezi reported a patent to US Application No. 62/756,467 pending. Dr. McLean reported a patent to US application pending. Our laboratory is a Waters Center of Innovation (Waters Corporation) and an Agilent Thought Leader laboratory. These relationships did not influence the research described in the present manuscript. Dr. Wargo reported "other" from Genentech, GlaxoSmithKline, BMS, Merck, Illumina, and personal fees from AstraZeneca outside the submitted work; in addition, Dr. Wargo had a patent to PCT/US17/53.717 issued, "MD Anderson." Dr. Greenberg reported grants from Juno Therapeutics and personal fees from Juno Therapeutics during the conduct of the study; personal fees from Rapt Therapeutics, Elpiscience, Celsius, and Nextech outside the submitted work; and had a patent to Juno Therapeutics licensed. Dr. Draetta reported personal fees from Biovelocita, Nurix, Blueprint Medicines, Frontier Medicines, Orionis Biosciences, Tessa Therapeutics, Helsinn, Forma Therapeutics, Symphogen, Alligator, Taiho Pharmaceutical Co., and FIRC Institute of Molecular Oncology outside the submitted work. No other disclosures were reported.

Submitted: 9 October 2019
Revised: 14 January 2020
Accepted: 19 March 2020

References

Angelin, A., L. Gil-de-Gómez, S. Dahiya, J. Jiao, L. Guo, M.H. Levine, Z. Wang, W.J. Quinn, III, P.K. Kopinski, L. Wang, et al. 2017. Foxp3 Reprograms T Cell Metabolism to Function in Low-Glucose, High-Lactate Environments. *Cell Metab.* 25:1282–1293.e7. https://doi.org/10.1016/j.cmet.2016.12.018

Aon, M.A., and A.K. Camara. 2015. Mitochondria: hubs of cellular signaling, energetics and redox balance. A rich, vibrant, and diverse landscape of mitochondrial research. *Front. Physiol.* 6:94. https://doi.org/10.3389/fphys.2015.00094

Aon, M.A., N. Bhatt, and S.C. Cortassa. 2014. Mitochondrial and cellular mechanisms for managing lipid excess. *Front. Physiol.* 5:282. https://doi.org/10.3389/fphys.2014.00282

Bailey, P., D.K. Chang, K. Nones, A.L. Johns, A.M. Patch, M.C. Gingras, D.K. Miller, A.N. Christ, T.J. Bruxner, M.C. Quinn, et al; Australian Pancreatic Cancer Genome Initiative. 2016. Genomic analyses identify molecular subtypes of pancreatic cancer. *Nature.* 531:47–52. https://doi.org/10.1038/nature16965

Beatty, G.L., and E.K. Moon. 2014. Chimeric antigen receptor T cells are vulnerable to immunosuppressive mechanisms present within the

tumor microenvironment. *OncoImmunology*. 3. e970027. https://doi.org/10.4161/21624011.2014.970027

Beatty, G.L., R. Winograd, R.A. Evans, K.B. Long, S.L. Luque, J.W. Lee, C. Clendenin, W.L. Gladney, D.M. Knoblock, P.D. Guirnalda, et al. 2015. Exclusion of T Cells From Pancreatic Carcinomas in Mice Is Regulated by Ly6C(low) F4/80(+) Extratumoral Macrophages. *Gastroenterology*. 149:201–210. https://doi.org/10.1053/j.gastro.2015.04.010

Berod, L., C. Friedrich, A. Nandan, J. Freitag, S. Hagemann, K. Harmrolfs, A. Sandouk, C. Hesse, C.N. Castro, H. Bähre, et al. 2014. De novo fatty acid synthesis controls the fate between regulatory T and T helper 17 cells. *Nat. Med.* 20:1327–1333. https://doi.org/10.1038/nm.3704

Brahmer, J.R., S.S. Tykodi, L.Q. Chow, W.J. Hwu, S.L. Topalian, P. Hwu, C.G. Drake, L.H. Camacho, J. Kauh, K. Odunsi, et al. 2012. Safety and activity of anti-PD-L1 antibody in patients with advanced cancer. *N. Engl. J. Med.* 366:2455–2465. https://doi.org/10.1056/NEJMoa1200694

Caprioli, R.M., T.B. Farmer, and J. Gile. 1997. Molecular imaging of biological samples: localization of peptides and proteins using MALDI-TOF MS. *Anal. Chem.* 69:4751–4760. https://doi.org/10.1021/ac970888i

Carstens, J.L., P. Correa de Sampaio, D. Yang, S. Barua, H. Wang, A. Rao, J.P. Allison, V.S. LeBleu, and R. Kalluri. 2017. Spatial computation of intratumoral T cells correlates with survival of patients with pancreatic cancer. *Nat. Commun.* 8:15095. https://doi.org/10.1038/ncomms15095

Casadonte, R., M. Kriegsmann, F. Zweynert, K. Friedrich, G. Baretton, M. Otto, S.O. Deininger, R. Paape, E. Belau, D. Suckau, et al. 2014. Imaging mass spectrometry to discriminate breast from pancreatic cancer metastasis in formalin-fixed paraffin-embedded tissues. *Proteomics*. 14: 956–964. https://doi.org/10.1002/pmic.201300430

Cham, C.M., and T.F. Gajewski. 2005. Glucose availability regulates IFN-gamma production and p70S6 kinase activation in CD8+ effector T cells. *J. Immunol.* 174:4670–4677. https://doi.org/10.4049/jimmunol.174.8.4670

Cham, C.M., G. Driessens, J.P. O'Keefe, and T.F. Gajewski. 2008. Glucose deprivation inhibits multiple key gene expression events and effector functions in CD8+ T cells. *Eur. J. Immunol.* 38:2438–2450. https://doi.org/10.1002/eji.200838289

Chang, C.H., J. Qiu, D. O'Sullivan, M.D. Buck, T. Noguchi, J.D. Curtis, Q. Chen, M. Gindin, M.M. Gubin, G.J. van der Windt, et al. 2015. Metabolic Competition in the Tumor Microenvironment Is a Driver of Cancer Progression. *Cell*. 162:1229–1241. https://doi.org/10.1016/j.cell.2015.08.016

Chen, M., J. Zhang, K. Sampieri, J.G. Clohessy, L. Mendez, E. Gonzalez-Billalabeitia, X.S. Liu, Y.R. Lee, J. Fung, J.M. Katon, et al. 2018. An aberrant SREBP-dependent lipogenic program promotes metastatic prostate cancer. *Nat. Genet.* 50:206–218. https://doi.org/10.1038/s41588-017-0027-2

Chong, J., O. Soufan, C. Li, I. Caraus, S. Li, G. Bourque, D.S. Wishart, and J. Xia. 2018. MetaboAnalyst 4.0: towards more transparent and integrative metabolomics analysis. *Nucleic Acids Res.* 46(W1):W486–W494. https://doi.org/10.1093/nar/gky310

Clark, C.E., S.R. Hingorani, R. Mick, C. Combs, D.A. Tuveson, and R.H. Vonderheide. 2007. Dynamics of the immune reaction to pancreatic cancer from inception to invasion. *Cancer Res.* 67:9518–9527. https://doi.org/10.1158/0008-5472.CAN-07-0175

Cornett, D.S., S.L. Frappier, and R.M. Caprioli. 2008. MALDI-FTICR imaging mass spectrometry of drugs and metabolites in tissue. *Anal. Chem.* 80: 5648–5653. https://doi.org/10.1021/ac800617s

De Monte, L., M. Reni, E. Tassi, D. Clavenna, I. Papa, H. Recalde, M. Braga, V. Di Carlo, C. Doglioni, and M.P. Protti. 2011. Intratumor T helper type 2 cell infiltrate correlates with cancer-associated fibroblast thymic stromal lymphopoietin production and reduced survival in pancreatic cancer. *J. Exp. Med.* 208:469–478. https://doi.org/10.1084/jem.20101876

de Pablo, M.A., S.A. Susin, E. Jacotot, N. Larochette, P. Costantini, L. Ravagnan, N. Zamzami, and G. Kroemer. 1999. Palmitate induces apoptosis via a direct effect on mitochondria. *Apoptosis*. 4:81–87. https://doi.org/10.1023/A:1009694124241

Diana, A., L.M. Wang, Z. D'Costa, P. Allen, A. Azad, M.A. Silva, Z. Soonawalla, S. Liu, W.G. McKenna, R.J. Muschel, et al. 2016. Prognostic value, localization and correlation of PD-1/PD-L1, CD8 and FOXP3 with the desmoplastic stroma in pancreatic ductal adenocarcinoma. *Oncotarget*. 7:40992–41004. https://doi.org/10.18632/oncotarget.10038

Eberlin, L.S., R.J. Tibshirani, J. Zhang, T.A. Longacre, G.J. Berry, D.B. Bingham, J.A. Norton, R.N. Zare, and G.A. Poultsides. 2014. Molecular assessment of surgical-resection margins of gastric cancer by mass-spectrometric imaging. *Proc. Natl. Acad. Sci. USA*. 111:2436–2441. https://doi.org/10.1073/pnas.1400274111

Ecker, C., and J.L. Riley. 2018. Translating In Vitro T Cell Metabolic Findings to In Vivo Tumor Models of Nutrient Competition. *Cell Metab.* 28: 190–195. https://doi.org/10.1016/j.cmet.2018.07.009

Ene-Obong, A., A.J. Clear, J. Watt, J. Wang, R. Fatah, J.C. Riches, J.F. Marshall, J. Chin-Aleong, C. Chelala, J.G. Gribben, et al. 2013. Activated pancreatic stellate cells sequester CD8+ T cells to reduce their infiltration of the juxtatumoral compartment of pancreatic ductal adenocarcinoma. *Gastroenterology*. 145:1121–1132. https://doi.org/10.1053/j.gastro.2013.07.025

Fahy, E., M. Sud, D. Cotter, and S. Subramaniam. 2007. LIPID MAPS online tools for lipid research. *Nucleic Acids Res.* 35(Web Server). W606-12. https://doi.org/10.1093/nar/gkm324

Fu, S., L. Yang, P. Li, O. Hofmann, L. Dicker, W. Hide, X. Lin, S.M. Watkins, A.R. Ivanov, and G.S. Hotamisligil. 2011. Aberrant lipid metabolism disrupts calcium homeostasis causing liver endoplasmic reticulum stress in obesity. *Nature*. 473:528–531. https://doi.org/10.1038/nature09968

Fukunaga, A., M. Miyamoto, Y. Cho, S. Murakami, Y. Kawarada, T. Oshikiri, K. Kato, T. Kurokawa, M. Suzuoki, Y. Nakakubo, et al. 2004. CD8+ tumor-infiltrating lymphocytes together with CD4+ tumor-infiltrating lymphocytes and dendritic cells improve the prognosis of patients with pancreatic adenocarcinoma. *Pancreas*. 28:e26–e31. https://doi.org/10.1097/00006676-200401000-00023

Gao, Q., and J.M. Goodman. 2015. The lipid droplet-a well-connected organelle. *Front. Cell Dev. Biol.* 3:49. https://doi.org/10.3389/fcell.2015.00049

Green, D.R., and J.C. Reed. 1998. Mitochondria and apoptosis. *Science*. 281: 1309–1312. https://doi.org/10.1126/science.281.5381.1309

Gruenbacher, G., and M. Thurnher. 2017. Mevalonate Metabolism in Immuno-Oncology. *Front. Immunol.* 8:1714. https://doi.org/10.3389/fimmu.2017.01714

Grüner, B.M., H. Hahne, P.K. Mazur, M. Trajkovic-Arsic, S. Maier, I. Esposito, E. Kalideris, C.W. Michalski, J. Kleeff, S. Rauser, et al. 2012. MALDI imaging mass spectrometry for in situ proteomic analysis of preneoplastic lesions in pancreatic cancer. *PLoS One*. 7. e39424. https://doi.org/10.1371/journal.pone.0039424

Guo, S., M. Contratto, G. Miller, L. Leichman, and J. Wu. 2017. Immunotherapy in pancreatic cancer: Unleash its potential through novel combinations. *World J. Clin. Oncol.* 8:230–240. https://doi.org/10.5306/wjco.v8.i3.230

Hankin, J.A., R.M. Barkley, and R.C. Murphy. 2007. Sublimation as a method of matrix application for mass spectrometric imaging. *J. Am. Soc. Mass Spectrom.* 18:1646–1652. https://doi.org/10.1016/j.jasms.2007.06.010

Hapala, I., E. Marza, and T. Ferreira. 2011. Is fat so bad? Modulation of endoplasmic reticulum stress by lipid droplet formation. *Biol. Cell.* 103: 271–285. https://doi.org/10.1042/BC20100144

Hingorani, S.R., E.F. Petricoin, A. Maitra, V. Rajapakse, C. King, M.A. Jacobetz, S. Ross, T.P. Conrads, T.D. Veenstra, B.A. Hitt, et al. 2003. Preinvasive and invasive ductal pancreatic cancer and its early detection in the mouse. *Cancer Cell*. 4:437–450. https://doi.org/10.1016/S1535-6108(03)00309-X

Hingorani, S.R., L. Wang, A.S. Multani, C. Combs, T.B. Deramaudt, R.H. Hruban, A.K. Rustgi, S. Chang, and D.A. Tuveson. 2005. Trp53R172H and KrasG12D cooperate to promote chromosomal instability and widely metastatic pancreatic ductal adenocarcinoma in mice. *Cancer Cell*. 7:469–483. https://doi.org/10.1016/j.ccr.2005.04.023

Ho, P.C., J.D. Bihuniak, A.N. Macintyre, M. Staron, X. Liu, R. Amezquita, Y.C. Tsui, G. Cui, G. Micevic, J.C. Perales, et al. 2015. Phosphoenolpyruvate Is a Metabolic Checkpoint of Anti-tumor T Cell Responses. *Cell*. 162: 1217–1228. https://doi.org/10.1016/j.cell.2015.08.012

Hori, M., M. Takahashi, N. Hiraoka, T. Yamaji, M. Mutoh, R. Ishigamori, K. Furuta, T. Okusaka, K. Shimada, T. Kosuge, et al. 2014. Association of pancreatic Fatty infiltration with pancreatic ductal adenocarcinoma. *Clin. Transl. Gastroenterol.* 5. e53. https://doi.org/10.1038/ctg.2014.5

Howie, D., S.P. Cobbold, E. Adams, A. Ten Bokum, A.S. Necula, W. Zhang, H. Huang, D.J. Roberts, B. Thomas, S.S. Hester, et al. 2017. Foxp3 drives oxidative phosphorylation and protection from lipotoxicity. *JCI Insight*. 2. e89160. https://doi.org/10.1172/jci.insight.89160

Hwang, H.K., H.I. Kim, S.H. Kim, J. Choi, C.M. Kang, K.S. Kim, and W.J. Lee. 2016. Prognostic impact of the tumor-infiltrating regulatory T-cell (Foxp3$^+$)/activated cytotoxic T lymphocyte (granzyme B$^+$) ratio on resected left-sided pancreatic cancer. *Oncol. Lett.* 12:4477–4484. https://doi.org/10.3892/ol.2016.5252

Ino, Y., R. Yamazaki-Itoh, K. Shimada, M. Iwasaki, T. Kosuge, Y. Kanai, and N. Hiraoka. 2013. Immune cell infiltration as an indicator of the immune microenvironment of pancreatic cancer. *Br. J. Cancer*. 108:914–923. https://doi.org/10.1038/bjc.2013.32

Jacobs, S.R., C.E. Herman, N.J. Maciver, J.A. Wofford, H.L. Wieman, J.J. Hammen, and J.C. Rathmell. 2008. Glucose uptake is limiting in T cell activation and requires CD28-mediated Akt-dependent and independent pathways. *J. Immunol.* 180:4476–4486. https://doi.org/10.4049/jimmunol.180.7.4476

Janes, P.W., S.C. Ley, A.I. Magee, and P.S. Kabouridis. 2000. The role of lipid rafts in T cell antigen receptor (TCR) signalling. *Semin. Immunol.* 12: 23–34. https://doi.org/10.1006/smim.2000.0204

Jang, J.E., C.H. Hajdu, C. Liot, G. Miller, M.L. Dustin, and D. Bar-Sagi. 2017. Crosstalk between Regulatory T Cells and Tumor-Associated Dendritic Cells Negates Anti-tumor Immunity in Pancreatic Cancer. *Cell Rep.* 20: 558–571. https://doi.org/10.1016/j.celrep.2017.06.062

Joyce, J.A., and D.T. Fearon. 2015. T cell exclusion, immune privilege, and the tumor microenvironment. *Science.* 348:74–80. https://doi.org/10.1126/science.aaa6204

Jury, E.C., F. Flores-Borja, and P.S. Kabouridis. 2007. Lipid rafts in T cell signalling and disease. *Semin. Cell Dev. Biol.* 18:608–615. https://doi.org/10.1016/j.semcdb.2007.08.002

Kim, H.E., A.R. Grant, M.S. Simic, R.A. Kohnz, D.K. Nomura, J. Durieux, C.E. Riera, M. Sanchez, E. Kapernick, S. Wolff, et al. 2016. Lipid Biosynthesis Coordinates a Mitochondrial-to-Cytosolic Stress Response. *Cell.* 166: 1539–1552.e16. https://doi.org/10.1016/j.cell.2016.08.027

Kishton, R.J., M. Sukumar, and N.P. Restifo. 2017. Metabolic Regulation of T Cell Longevity and Function in Tumor Immunotherapy. *Cell Metab.* 26:94–109. https://doi.org/10.1016/j.cmet.2017.06.016

Köberlin, M.S., B. Snijder, L.X. Heinz, C.L. Baumann, A. Fauster, G.I. Vladimer, A.C. Gavin, and G. Superti-Furga. 2015. A Conserved Circular Network of Coregulated Lipids Modulates Innate Immune Responses. *Cell.* 162:170–183. https://doi.org/10.1016/j.cell.2015.05.051

Lesmana, C.R., L.S. Pakasi, S. Inggriani, M.L. Aidawati, and L.A. Lesmana. 2015. Development of non-alcoholic fatty liver disease scoring system among adult medical check-up patients: a large cross-sectional and prospective validation study. *Diabetes Metab. Syndr. Obes.* 8:213–218. https://doi.org/10.2147/DMSO.S80364

Liberzon, A., C. Birger, H. Thorvaldsdóttir, M. Ghandi, J.P. Mesirov, and P. Tamayo. 2015. The Molecular Signatures Database (MSigDB) hallmark gene set collection. *Cell Syst.* 1:417–425. https://doi.org/10.1016/j.cels.2015.12.004

Lingwood, D., and K. Simons. 2010. Lipid rafts as a membrane-organizing principle. *Science.* 327:46–50. https://doi.org/10.1126/science.1174621

Listenberger, L.L., X. Han, S.E. Lewis, S. Cases, R.V. Farese, Jr., D.S. Ory, and J.E. Schaffer. 2003. Triglyceride accumulation protects against fatty acid-induced lipotoxicity. *Proc. Natl. Acad. Sci. USA.* 100:3077–3082. https://doi.org/10.1073/pnas.0630588100

Liyanage, U.K., T.T. Moore, H.G. Joo, Y. Tanaka, V. Herrmann, G. Doherty, J.A. Drebin, S.M. Strasberg, T.J. Eberlein, P.S. Goedegebuure, et al. 2002. Prevalence of regulatory T cells is increased in peripheral blood and tumor microenvironment of patients with pancreas or breast adenocarcinoma. *J. Immunol.* 169:2756–2761. https://doi.org/10.4049/jimmunol.169.5.2756

Lodhi, I.J., and C.F. Semenkovich. 2014. Peroxisomes: a nexus for lipid metabolism and cellular signaling. *Cell Metab.* 19:380–392. https://doi.org/10.1016/j.cmet.2014.01.002

Love, M.I., W. Huber, and S. Anders. 2014. Moderated estimation of fold change and dispersion for RNA-seq data with DESeq2. *Genome Biol.* 15: 550. https://doi.org/10.1186/s13059-014-0550-8

Martin, G.S.. 2003. Cell signaling and cancer. *Cancer Cell.* 4:167–174. https://doi.org/10.1016/S1535-6108(03)00216-2

McAllister, F., J.M. Bailey, J. Alsina, C.J. Nirschl, R. Sharma, H. Fan, Y. Rattigan, J.C. Roeser, R.H. Lankapalli, H. Zhang, et al. 2014. Oncogenic Kras activates a hematopoietic-to-epithelial IL-17 signaling axis in preinvasive pancreatic neoplasia. *Cancer Cell.* 25:621–637. https://doi.org/10.1016/j.ccr.2014.03.014

Mellman, I., G. Coukos, and G. Dranoff. 2011. Cancer immunotherapy comes of age. *Nature.* 480:480–489. https://doi.org/10.1038/nature10673

Menon, S., S. Shin, and G. Dy. 2016. Advances in Cancer Immunotherapy in Solid Tumors. *Cancers (Basel).* 8:106. https://doi.org/10.3390/cancers8120106

Messina, A., S. Reina, F. Guarino, A. Magrì, F. Tomasello, R.E. Clark, R.R. Ramsay, and V. De Pinto. 2014. Live cell interactome of the human voltage dependent anion channel 3 (VDAC3) revealed in HeLa cells by affinity purification tag technique. *Mol. Biosyst.* 10:2134–2145. https://doi.org/10.1039/C4MB00237G

Molina, J.R., Y. Sun, M. Protopopova, S. Gera, M. Bandi, C. Bristow, T. McAfoos, P. Morlacchi, J. Ackroyd, A.A. Agip, et al. 2018. An inhibitor of oxidative phosphorylation exploits cancer vulnerability. *Nat. Med.* 24: 1036–1046. https://doi.org/10.1038/s41591-018-0052-4

Mukherjee, P., A.R. Ginardi, C.S. Madsen, T.L. Tinder, F. Jacobs, J. Parker, B. Agrawal, B.M. Longenecker, and S.J. Gendler. 2001. MUC1-specific CTLs are non-functional within a pancreatic tumor microenvironment. *Glycoconj. J.* 18:931–942. https://doi.org/10.1023/A:1022260711583

Murai, T.. 2012. The role of lipid rafts in cancer cell adhesion and migration. *Int. J. Cell Biol.* 2012. 763283. https://doi.org/10.1155/2012/763283

Nguyen, T.B., and J.A. Olzmann. 2017. Lipid droplets and lipotoxicity during autophagy. *Autophagy.* 13:2002–2003. https://doi.org/10.1080/15548627.2017.1359451

Nieman, K.M., H.A. Kenny, C.V. Penicka, A. Ladanyi, R. Buell-Gutbrod, M.R. Zillhardt, I.L. Romero, M.S. Carey, G.B. Mills, G.S. Hotamisligil, et al. 2011. Adipocytes promote ovarian cancer metastasis and provide energy for rapid tumor growth. *Nat. Med.* 17:1498–1503. https://doi.org/10.1038/nm.2492

O'Sullivan, D., G.J. van der Windt, S.C. Huang, J.D. Curtis, C.H. Chang, M.D. Buck, J. Qiu, A.M. Smith, W.Y. Lam, L.M. DiPlato, et al. 2014. Memory CD8(+) T cells use cell-intrinsic lipolysis to support the metabolic programming necessary for development. *Immunity.* 41:75–88. https://doi.org/10.1016/j.immuni.2014.06.005

Ogilvie, R.F.. 1933. The islands of Langerhans in 19 cases of obesity. *J. Pathol.* 37:473–481. https://doi.org/10.1002/path.1700370314

Pacella, I., C. Procaccini, C. Focaccetti, S. Miacci, E. Timperi, D. Faicchia, M. Severa, F. Rizzo, E.M. Coccia, F. Bonacina, et al. 2018. Fatty acid metabolism complements glycolysis in the selective regulatory T cell expansion during tumor growth. *Proc. Natl. Acad. Sci. USA.* 115: E6546–E6555. https://doi.org/10.1073/pnas.1720113115

Plötz, T., M. Hartmann, S. Lenzen, and M. Elsner. 2016. The role of lipid droplet formation in the protection of unsaturated fatty acids against palmitic acid induced lipotoxicity to rat insulin-producing cells. *Nutr. Metab. (Lond.).* 13:16. https://doi.org/10.1186/s12986-016-0076-z

Prentice, B.M., N.J. Hart, N. Phillips, R. Haliyur, A. Judd, R. Armandala, J.M. Spraggins, C.L. Lowe, K.L. Boyd, R.W. Stein, et al. 2019. Imaging mass spectrometry enables molecular profiling of mouse and human pancreatic tissue. *Diabetologia.* 62:1036–1047. https://doi.org/10.1007/s00125-019-4855-8

Procaccini, C., F. Carbone, D. Di Silvestre, F. Brambilla, V. De Rosa, M. Galgani, D. Faicchia, G. Marone, D. Tramontano, M. Corona, et al. 2016. The Proteomic Landscape of Human Ex Vivo Regulatory and Conventional T Cells Reveals Specific Metabolic Requirements. *Immunity.* 44:406–421. https://doi.org/10.1016/j.immuni.2016.01.028

Protti, M.P., and L. De Monte. 2013. Immune infiltrates as predictive markers of survival in pancreatic cancer patients. *Front. Physiol.* 4:210. https://doi.org/10.3389/fphys.2013.00210

Schaefer, J.H.. 1926. The normal weight of the pancreas in the adult human being: A biometric study. *Anat. Rec.* 32:119–132. https://doi.org/10.1002/ar.1090320204

Scharping, N.E., A.V. Menk, R.S. Moreci, R.D. Whetstone, R.E. Dadey, S.C. Watkins, R.L. Ferris, and G.M. Delgoffe. 2016. The Tumor Microenvironment Represses T Cell Mitochondrial Biogenesis to Drive Intratumoral T Cell Metabolic Insufficiency and Dysfunction. *Immunity.* 45: 374–388. https://doi.org/10.1016/j.immuni.2016.07.009

Schrimpe-Rutledge, A.C., S.G. Codreanu, S.D. Sherrod, and J.A. McLean. 2016. Untargeted Metabolomics Strategies-Challenges and Emerging Directions. *J. Am. Soc. Mass Spectrom.* 27:1897–1905. https://doi.org/10.1007/s13361-016-1469-y

Sena, L.A., S. Li, A. Jairaman, M. Prakriya, T. Ezponda, D.A. Hildeman, C.R. Wang, P.T. Schumacker, J.D. Licht, H. Perlman, et al. 2013. Mitochondria are required for antigen-specific T cell activation through reactive oxygen species signaling. *Immunity.* 38:225–236. https://doi.org/10.1016/j.immuni.2012.10.020

Shao, W., and P.J. Espenshade. 2012. Expanding roles for SREBP in metabolism. *Cell Metab.* 16:414–419. https://doi.org/10.1016/j.cmet.2012.09.002

Sharma, R.B., and L.C. Alonso. 2014. Lipotoxicity in the pancreatic beta cell: not just survival and function, but proliferation as well? *Curr. Diab. Rep.* 14:492. https://doi.org/10.1007/s11892-014-0492-2

Shen, T., L. Zhou, H. Shen, C. Shi, S. Jia, G.P. Ding, and L. Cao. 2017. Prognostic value of programmed cell death protein 1 expression on CD8+ T lymphocytes in pancreatic cancer. *Sci. Rep.* 7:7848. https://doi.org/10.1038/s41598-017-08479-9

Shinjo, S., S. Jiang, M. Nameta, T. Suzuki, M. Kanai, Y. Nomura, and N. Goda. 2017. Disruption of the mitochondria-associated ER membrane (MAM) plays a central role in palmitic acid-induced insulin resistance. *Exp. Cell Res.* 359:86–93. https://doi.org/10.1016/j.yexcr.2017.08.006

Siska, P.J., and J.C. Rathmell. 2015. T cell metabolic fitness in antitumor immunity. *Trends Immunol.* 36:257–264. https://doi.org/10.1016/j.it.2015.02.007

Smits, M.M., and E.J. van Geenen. 2011. The clinical significance of pancreatic steatosis. *Nat. Rev. Gastroenterol. Hepatol.* 8:169–177. https://doi.org/10.1038/nrgastro.2011.4

Spiekerkoetter, U., B. Sun, Z. Khuchua, M.J. Bennett, and A.W. Strauss. 2003. Molecular and phenotypic heterogeneity in mitochondrial trifunctional protein deficiency due to beta-subunit mutations. *Hum. Mutat.* 21:598–607. https://doi.org/10.1002/humu.10211

Strohalm, M., M. Hassman, B. Kosata, and M. Kodícek. 2008. mMass data miner: an open source alternative for mass spectrometric data analysis. *Rapid Commun. Mass Spectrom.* 22:905–908. https://doi.org/10.1002/rcm.3444

Stromnes, I.M., T.M. Schmitt, A. Hulbert, J.S. Brockenbrough, H. Nguyen, C. Cuevas, A.M. Dotson, X. Tan, J.L. Hotes, P.D. Greenberg, et al. 2015. T Cells Engineered against a Native Antigen Can Surmount Immunologic and Physical Barriers to Treat Pancreatic Ductal Adenocarcinoma. *Cancer Cell.* 28:638–652. https://doi.org/10.1016/j.ccell.2015.09.022

Subramanian, A., P. Tamayo, V.K. Mootha, S. Mukherjee, B.L. Ebert, M.A. Gillette, A. Paulovich, S.L. Pomeroy, T.R. Golub, E.S. Lander, et al. 2005. Gene set enrichment analysis: a knowledge-based approach for interpreting genome-wide expression profiles. *Proc. Natl. Acad. Sci. USA.* 102:15545–15550. https://doi.org/10.1073/pnas.0506580102

Sukumar, M., R. Roychoudhuri, and N.P. Restifo. 2015. Nutrient Competition: A New Axis of Tumor Immunosuppression. *Cell.* 162:1206–1208. https://doi.org/10.1016/j.cell.2015.08.064

Takahashi, M., M. Hori, R. Ishigamori, M. Mutoh, T. Imai, and H. Nakagama. 2018. Fatty pancreas: A possible risk factor for pancreatic cancer in animals and humans. *Cancer Sci.* 109:3013–3023. https://doi.org/10.1111/cas.13766

Thiam, A.R., and M. Beller. 2017. The why, when and how of lipid droplet diversity. *J. Cell Sci.* 130:315–324. https://doi.org/10.1242/jcs.192021

Tomita, Y., K. Azuma, Y. Nonaka, Y. Kamada, M. Tomoeda, M. Kishida, M. Tanemura, and E. Miyoshi. 2014. Pancreatic fatty degeneration and fibrosis as predisposing factors for the development of pancreatic ductal adenocarcinoma. *Pancreas.* 43:1032–1041. https://doi.org/10.1097/MPA.0000000000000159

Tucci, S., D. Herebian, M. Sturm, A. Seibt, and U. Spiekerkoetter. 2012. Tissue-specific strategies of the very-long chain acyl-CoA dehydrogenase-deficient (VLCAD-/-) mouse to compensate a defective fatty acid β-oxidation. *PLoS One.* 7. e45429. https://doi.org/10.1371/journal.pone.0045429

Ulloth, J.E., C.A. Casiano, and M. De Leon. 2003. Palmitic and stearic fatty acids induce caspase-dependent and -independent cell death in nerve growth factor differentiated PC12 cells. *J. Neurochem.* 84:655–668. https://doi.org/10.1046/j.1471-4159.2003.01571.x

van der Windt, G.J.W., C.H. Chang, and E.L. Pearce. 2016. Measuring Bioenergetics in T Cells Using a Seahorse Extracellular Flux Analyzer. *Curr. Protoc. Immunol.* 113:1–: 14. https://doi.org/10.1002/0471142735.im0316bs113

van der Windt, G.J., B. Everts, C.H. Chang, J.D. Curtis, T.C. Freitas, E. Amiel, E.J. Pearce, and E.L. Pearce. 2012. Mitochondrial respiratory capacity is a critical regulator of CD8+ T cell memory development. *Immunity.* 36:68–78. https://doi.org/10.1016/j.immuni.2011.12.007

Vander Heiden, M.G., L.C. Cantley, and C.B. Thompson. 2009. Understanding the Warburg effect: the metabolic requirements of cell proliferation. *Science.* 324:1029–1033. https://doi.org/10.1126/science.1160809

Vevea, J.D., E.J. Garcia, R.B. Chan, B. Zhou, M. Schultz, G. Di Paolo, J.M. McCaffery, and L.A. Pon. 2015. Role for Lipid Droplet Biogenesis and Microlipophagy in Adaptation to Lipid Imbalance in Yeast. *Dev. Cell.* 35:584–599. https://doi.org/10.1016/j.devcel.2015.11.010

Wanders, R.J., P. Vreken, M.E. den Boer, F.A. Wijburg, A.H. van Gennip, and L. IJlst. 1999. Disorders of mitochondrial fatty acyl-CoA beta-oxidation. *J. Inherit. Metab. Dis.* 22:442–487. https://doi.org/10.1023/A:1005504223140

Wei, J., J. Raynor, T.L. Nguyen, and H. Chi. 2017. Nutrient and Metabolic Sensing in T Cell Responses. *Front. Immunol.* 8:247. https://doi.org/10.3389/fimmu.2017.00247

Welte, M.A.. 2015. Expanding roles for lipid droplets. *Curr. Biol.* 25:R470–R481. https://doi.org/10.1016/j.cub.2015.04.004

Wherry, E.J., and M. Kurachi. 2015. Molecular and cellular insights into T cell exhaustion. *Nat. Rev. Immunol.* 15:486–499. https://doi.org/10.1038/nri3862

Wherry, E.J., S.J. Ha, S.M. Kaech, W.N. Haining, S. Sarkar, V. Kalia, S. Subramaniam, J.N. Blattman, D.L. Barber, and R. Ahmed. 2007. Molecular signature of CD8+ T cell exhaustion during chronic viral infection. *Immunity.* 27:670–684. https://doi.org/10.1016/j.immuni.2007.09.006

Winograd, R., K.T. Byrne, R.A. Evans, P.M. Odorizzi, A.R. Meyer, D.L. Bajor, C. Clendenin, B.Z. Stanger, E.E. Furth, E.J. Wherry, et al. 2015. Induction of T-cell Immunity Overcomes Complete Resistance to PD-1 and CTLA-4 Blockade and Improves Survival in Pancreatic Carcinoma. *Cancer Immunol. Res.* 3:399–411. https://doi.org/10.1158/2326-6066.CIR-14-0215

Yang, W., Y. Bai, Y. Xiong, J. Zhang, S. Chen, X. Zheng, X. Meng, L. Li, J. Wang, C. Xu, et al. 2016. Potentiating the antitumour response of CD8(+) T cells by modulating cholesterol metabolism. *Nature.* 531:651–655. https://doi.org/10.1038/nature17412

Zhang, Y., R. Kurupati, L. Liu, X.Y. Zhou, G. Zhang, A. Hudaihed, F. Filisio, W. Giles-Davis, X. Xu, G.C. Karakousis, et al. 2017. Enhancing CD8$^+$ T Cell Fatty Acid Catabolism within a Metabolically Challenging Tumor Microenvironment Increases the Efficacy of Melanoma Immunotherapy. *Cancer Cell.* 32:377–391.e9. https://doi.org/10.1016/j.ccell.2017.08.004

Zhang, Y., W. Yan, E. Mathew, F. Bednar, S. Wan, M.A. Collins, R.A. Evans, T.H. Welling, R.H. Vonderheide, and M.P. di Magliano. 2014. CD4+ T lymphocyte ablation prevents pancreatic carcinogenesis in mice. *Cancer Immunol. Res.* 2:423–435. https://doi.org/10.1158/2326-6066.CIR-14-0016-T

JEM

Supplemental material

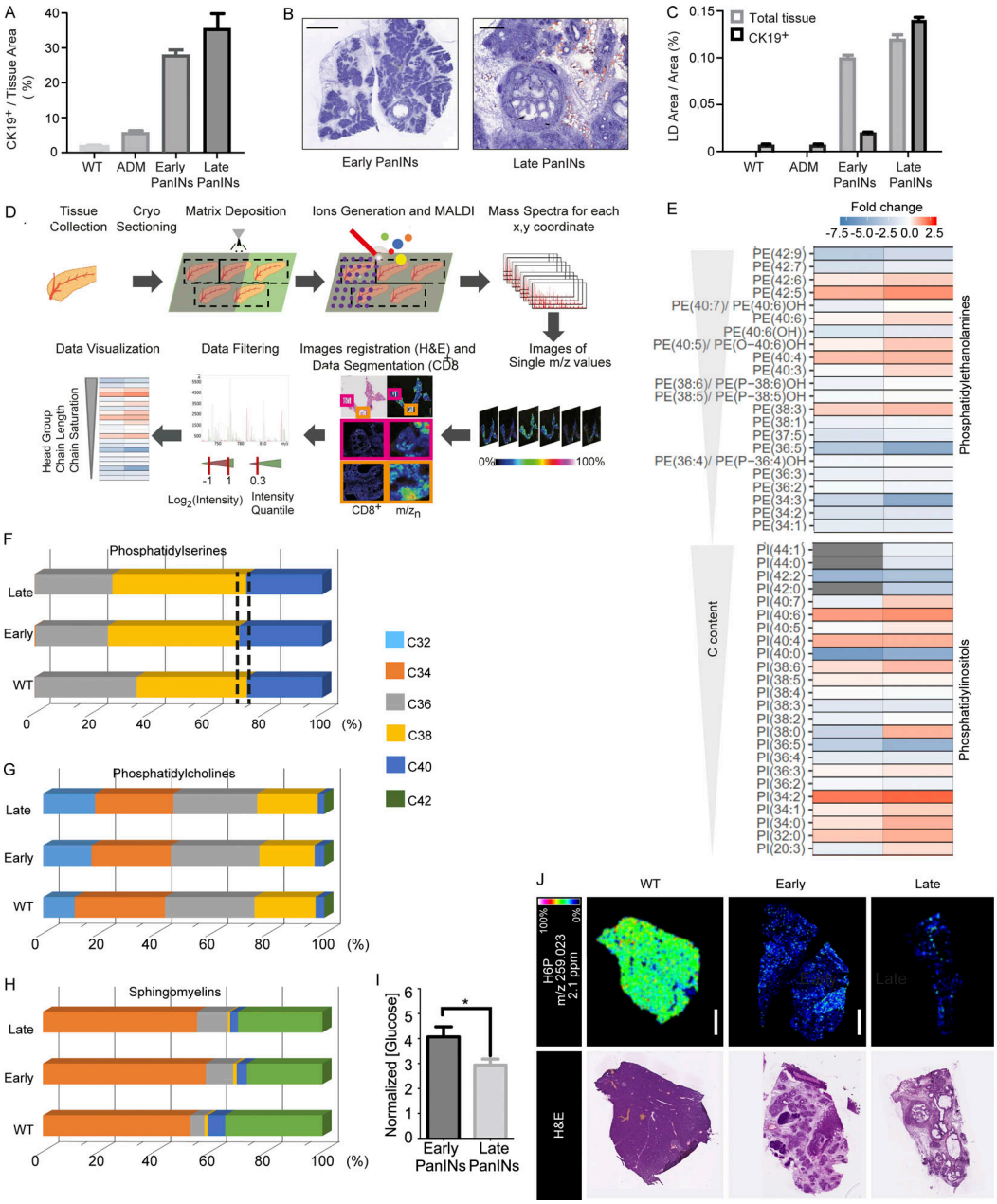

Figure S1. **Lipids accumulate in PDA TME while glucose and H6Ps decreases during PDA progression.** Related to Fig. 1. **(A)** Quantification by immunofluorescence of CK19⁺ area at indicated time points expressed as percentage over the total tissue area. Results are expressed as mean ± SE of three different areas on three independent pancreatic samples. **(B)** Representative images of Red Oil staining of murine early (left) and late (right) PanINs (n = 3). Red arrowheads highlight Red Oil–positive areas. Scale bar = 2 mm (left); 0.5 mm (right). **(C)** Quantification by immunofluorescence of neutral lipids area at indicated time points expressed as percentage of LipidTOX-positive over total tissue or tumor (CK19⁺) area. Results are indicative of three different areas on three independent pancreatic samples. **(D)** IMS workflow. Frozen pancreata were sectioned at 10-µm thickness on a gold-coated stainless steel target for IMS. IMS was performed on either a 15T or 9.4T SolariX FT-ICR mass spectrometer in positive or negative ion mode from m/z 500 to 2,000 with a 75-µm raster step, generating a mass spectrum at each pixel. The data were segmented in SCiLS through k-means clustering and a segment that best matched CD8⁺ staining. A mean spectrum was then generated for these segments. The peak list of each segment was searched against the LIPID MAPS database, and mean intensity values for each accurate mass lipid identification were extracted. Through a home-built script in R, data were filtered for visualization by retaining only those lipids with sufficient signal-to-noise ratios and that represented large fold changes between time points. This was done by filtering out log2(intensity) values between −1 and 1 and intensity values <0.3 of the quantile in the control group. Data were then visualized in a heatmap format sorted by head group, fatty acyl chain length, and level of fatty acyl chain unsaturation. **(E)** Heatmap representations of a series of PEs and PIs showing changes in lipid intensity in KC mice at early and late stages of disease compared with the pancreas of a control mouse. **(F–H)** Bar plots show the relative fraction of lipids of various FA chain lengths detected at the different disease time points for the indicated lipids (FAs for the three lipid types were summed). The scale for color code is above. **(I)** Quantification of extracellular glucose in murine early (black) and late (gray) PanINs. Free glucose was measured using a colorimetric-based assay and then normalized based on the weight of the fresh tissue. Each group includes 10 mice. Error bars represent mean ± SEM. Statistics were calculated using an unpaired two-tailed Student's t test; *, P ≤ 0.05–0.01. **(J)** IMS intensity distributions on the same tissues presented in Fig. 1 A show that H6Ps (false-color rainbow images displayed without normalization) decrease moving from earlier to late time points (n = 2). Scale bar = 2 mm.

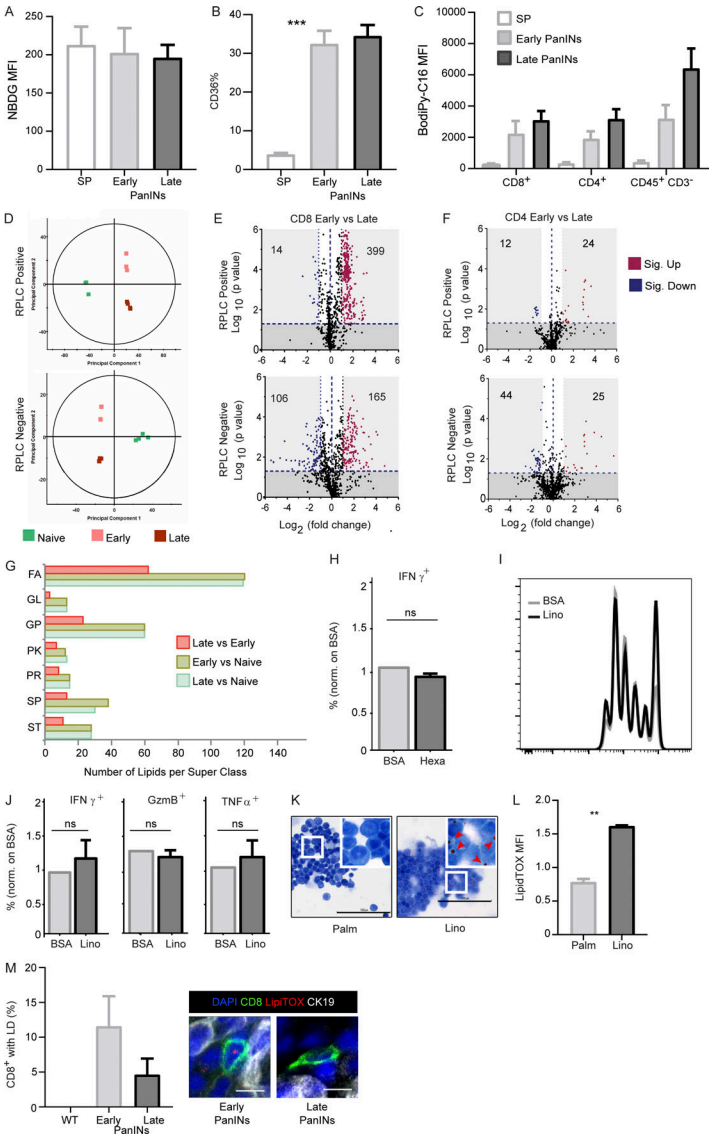

Figure S2. **VLCFA accumulation in intrapancreatic CD8⁺ T cells.** Related to Fig. 3. **(A)** Bar graph shows the quantification of the 2-NBDG used to monitor in vivo glucose uptake in early (gray bar, *n* = 6) and late (black bar, *n* = 8) PanINs infiltrating CD8⁺ T cells compared with control splenic CD8⁺ T cells (white bar, *n* = 9). Numbers indicate the MFI. **(B)** CD36 expression in early (gray bar, *n* = 13) and late (black bar, *n* = 9) PanINs infiltrating CD8⁺ T cells compared with control splenic CD8⁺ T cells (white bar, *n* = 9). Numbers indicate percentages of CD36⁺ cells inside the CD3⁺CD8⁺ gate. **(C)** Bar graph showing the quantification of the Bodipy-C_{16} in CD4⁺, CD8⁺, CD45⁺CD3⁻ cells infiltrating early (gray bar, *n* = 3) and late (black bar, *n* = 9) PanINs compared with relative control splenic populations (white bar, *n* = 9). Numbers indicate MFI. **(D)** Supervised PCA (partial least squares discriminant analysis) plots from liquid chromatography–MS performed on intrapancreatic CD8⁺ and CD4⁺ T cells flow-sorted from early (*n* = 3) and late (*n* = 3) PanINs. Naive T cells were used as control (*n* = 3). Results from RPLC-positive (upper) and negative (bottom) mode are represented. Partial least squares discriminant analysis plots (univariate scaling, performed in EZ Info from data generated in Progenesis QI v2) use abundance levels for all metabolite species within a sample across to determine the principal axes of abundance variation. Presenting the abundance data in PC space allows us to distinguish different metabolic profiles between the three sample groups. **(E and F)** Volcano plot representing changes of detected compounds in early versus late PanINs in intrapancreatic CD8⁺ (E) and CD4⁺ (F) T cells. Numbers of peaks that met significant criteria ($P \leq 0.05$, fold change $\geq|2|$) are indicated. Total number of compounds detected: 1,157 (RPLC-positive mode) and 1,302 (RPLC-negative mode). **(G)** Statistically different lipid metabolic compounds detected in CD8⁺ T cells over the time course of disease progression, suggesting a general increase of lipids (at the superclass level), and in particular FAs. The positive and negative data were coupled together and filtered by significance criteria, and redundancy was removed from the compound identification (m/z_RT) and from the chemical formula to narrow down to one lipid compound (level 3) identification. See legend for color code. **(H–J)** T cells activated with αCD3/αCD28 with 100 µM hexanoic (H, black; *n* = 5) or BSA-linoleic acid (I and J, black; *n* = 10) or BSA (as control, gray) for 72 h. Data were normalized on BSA. **(I and J)** Carboxyfluorescein succinimidyl ester profile (I) and bar graphs (H and J) showing percentages of effector cytokines in Lino-treated (J) or hexanoic acid–treated (H) CD8⁺ T cells normalized on BSA control cells. **(K)** Representative images of CD8⁺ T cells treated with BSA-linoleic (right) or BSA-palmitic (left). After cytospin, cells were stained with Red Oil to highlight neutral lipids. Red arrowheads indicate LDs. Scale bar = 100 µm. **(L)** Quantification of neutral lipids by LipidTOX staining on CD8⁺ T cells treated with BSA-linoleic (right) or BSA-palmitic (left). BSA-treated cells were used as controls. Results are indicative of three independent experiments with a total of eight different mice. **(M)** Quantification by LipidTOX immunofluorescence of neutral lipids at indicated time points expressed as percentage of CD8⁺ T cells that contain at least one LD. Results are indicative of three different areas on three independent pancreatic samples. Scale bar = 20 µm. In all graphs, error bars represent mean ± SEM. Statistic was calculated using a two-tailed Student's *t* test; **, $P \leq 0.01$–0.001; ***, $P \leq 0.001$–0.0001; ns, not significant.

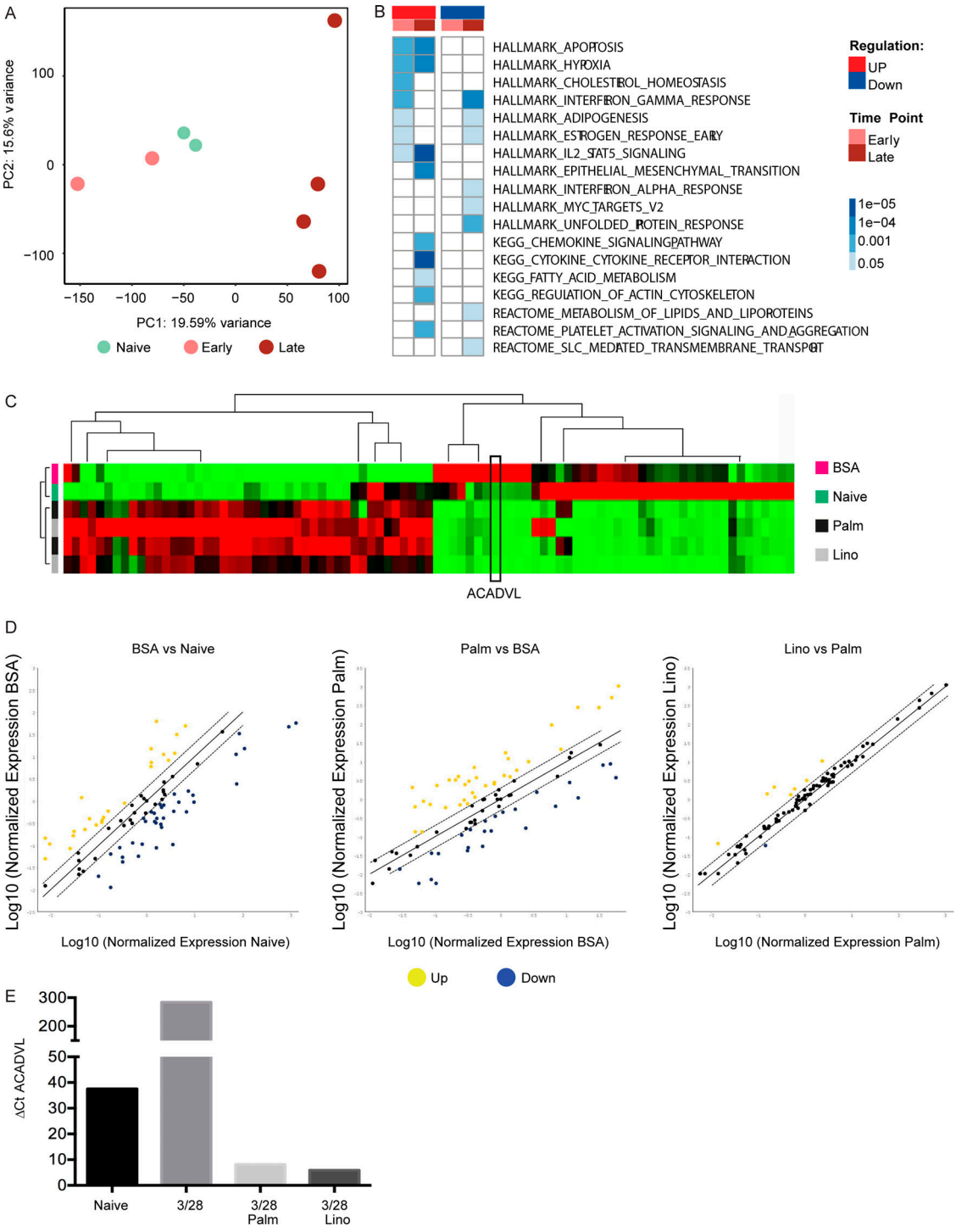

Figure S3. **Intrapancreatic CD8⁺ T cells from early and late lesions are transcriptionally distinct.** Related to Fig. 5. **(A)** PCA of the transcriptome of intrapancreatic CD8⁺ T cells flow sorted from WT or KC mice at indicated ages (n = 3, see color code in the figure). **(B)** Gene ontology analysis was performed against the Molecular Signatures Database, using Investigate Gene Sets web program under GSEA. Prediction of activated (UP, red) or inactivated (DOWN, blue) signatures are indicated for early (pink) and late (brown) PanINs. Scale indicates P values. **(C)** Nonsupervised hierarchical clustering of the entire dataset (n = 84) to display a heatmap with dendrograms indicating coregulated genes across the indicated groups (n = 2). Green, minimal expression; black, average expression; red, maximal expression. **(D)** Scatter plots comparing the normalized expression of every gene on the array between the two indicated groups. The central line indicates unchanged gene expression, and the dotted lines indicate the fold regulation threshold (1.3). Data points beyond dotted lines in the upper left (yellow) and lower right (blue) sections meet the selected fold regulation threshold. **(E)** ACADVL expression expressed as ΔCt across the different indicated groups.

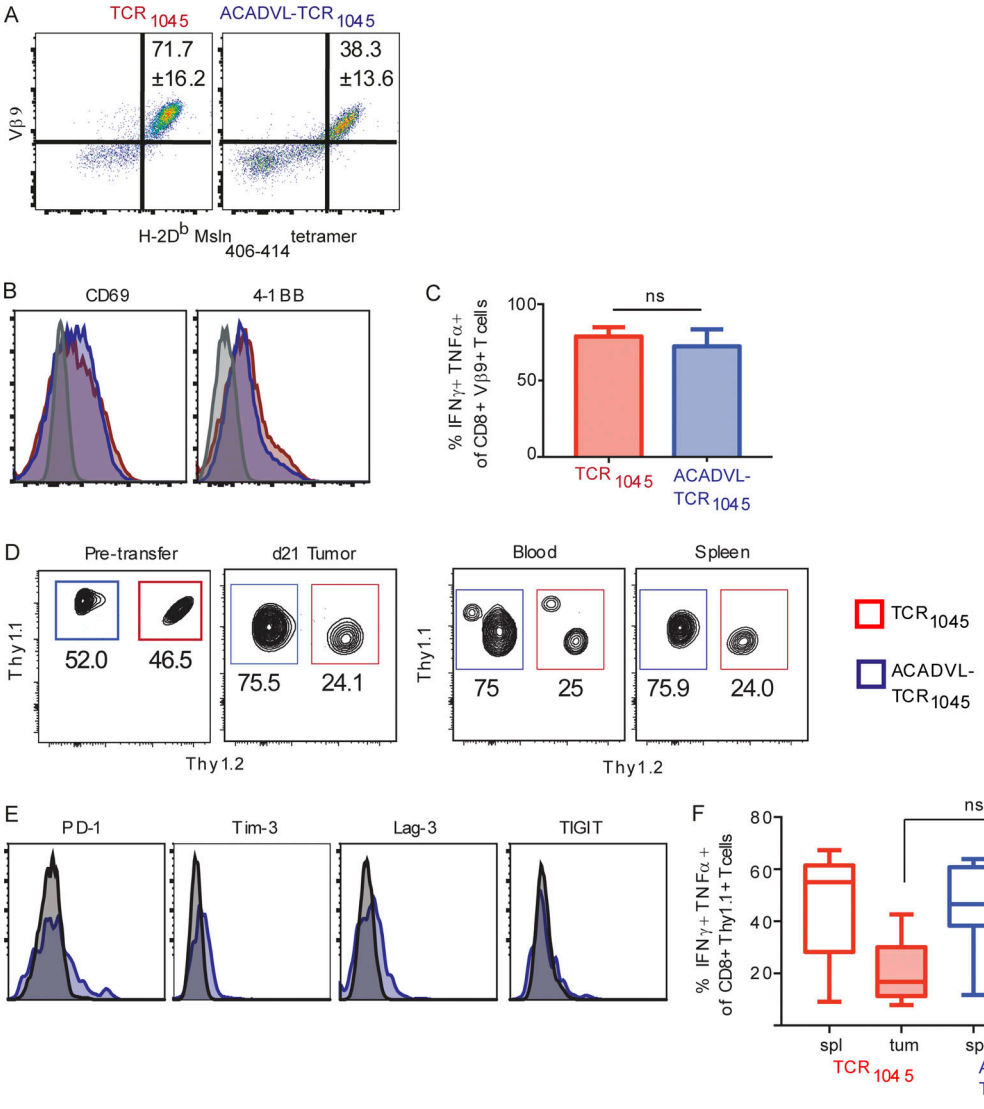

Figure S4. **ACADVL overexpression confers enhanced metabolic fitness.** Related to Fig. 6. **(A)** Transduction efficiency, gated on live CD8⁺ Thy1.1⁺. **(B)** Expression of the indicated activation receptors on transduced cells, gated on live CD8⁺ Thy1.1⁺ Vβ9⁺ cells. The gray histogram represents naive P14 staining, the red histogram represents TCR_{1045}-transduced T cells, and the blue histogram represents ACADVL-TCR_{1045} transduced T cells. Data are representative of three independent experiments. **(C)** Production of IFNγ and TNFα by TCR_{1045} T (red) and ACADVL-TCR_{1045} T cells (blue) 7 d after activation and transduction, stimulated with $Msln_{406–414}$ peptide for 5 h. **(D)** Proportions of cotransferred TCR_{1045} T (red) and ACADVL-TCR_{1045} T cells (blue) before and after transfer (day 21) in tumor, blood, or spleen, gated on live CD8⁺ Thy1.1⁺ cells. Plots are representative of four independent experiments. **(E)** Inhibitory receptor expression on engineered cells isolated from tumor at day 10, gated on live CD8⁺ Thy1.1⁺ Vβ9⁺ cells. The gray histogram represents naive P14 staining, and the blue histogram represents ACADVL-$TCR_{1,045}$–transduced T cells. **(F)** Ex vivo production of IFNγ and TNFα by TCR_{1045} T (red) and ACADVL-TCR_{1045} T cells (blue) isolated from the spleen (SP) or tumor (tum) 10 d after transfer and stimulated for 5 h with $Msln_{406–414}$ peptide. Data are representative of four independent experiments. In all graphs, error bars represent mean ± SEM. Statistic was calculated using a two-tailed Student's *t* test; ns, not significant.

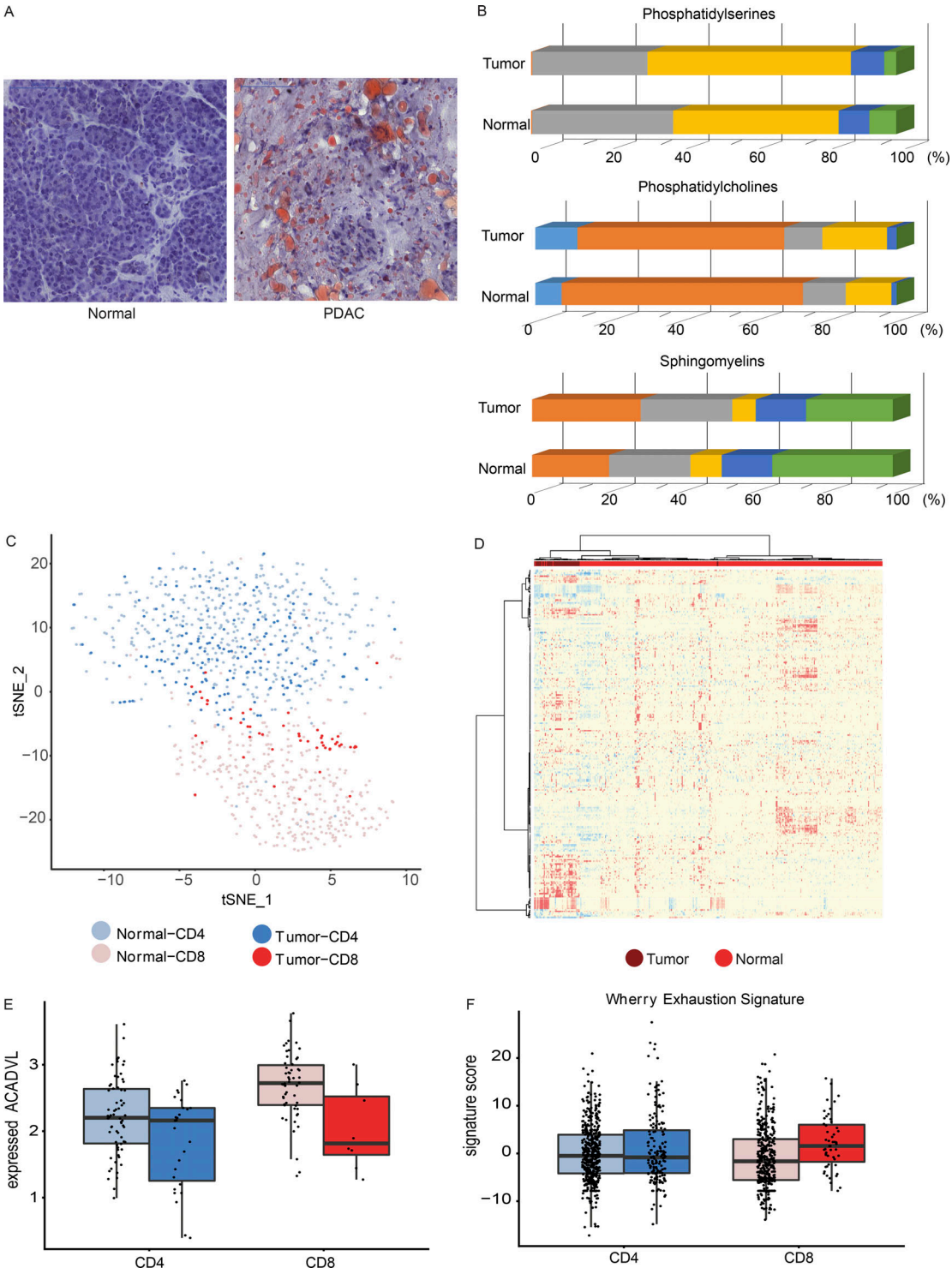

Figure S5. **Lipid accumulation and ACADVL dysfunction in human CD8+ T cells infiltrating PDA.** Related to Fig. 7. **(A)** Representative images of Red Oil staining of seven matched human PDA and normal adjacent tissue. Bar = 100 µm. **(B)** Bar plots showing the relative fraction of lipids of various FA chain lengths detected at the different disease time points for phosphatidylserine (upper), PC (center), and sphingomyelins (lower; FAs for the three lipid types were summed). **(C)** t-Distributed stochastic neighbor embedding (tSNE) plot of intrapancreatic $CD8^+$ (red) and $CD4^+$ (blue) T cells from human PDA samples (dark color, $n = 4$) and adjacent normal tissues (light color, $n = 4$). **(D)** Unsupervised clustering analysis of the single-cell transcriptome of human intrapancreatic $CD8^+$ T cells from human PDA samples (dark red, $n = 4$) and adjacent normal tissues (light red, $n = 4$) showing how intratumoral $CD8^+$ T cells cluster together. Each column represents a cell. **(E)** Box-and-whiskers plot representing ACADVL expression in human intrapancreatic $CD8^+$ (red) and $CD4^+$ (blue) T cells from human PDA samples (dark colors, $n = 4$) and adjacent normal tissues (colors, $n = 4$). Only actual values from cells expressing the gene are included. Permutation test from median differences highlights significant differences between $CD8^+$ groups ($P = 0.00033$) but not for $CD4^+$ groups ($P = 0.347$). **(F)** Exhaustion score based on previously published transcriptomic signature (Wherry et al., 2007). Wilcoxon test for tumor versus normal comparison: $P = 0.00028$ for $CD8^+$ T cells and $P = 0.6422$ for $CD4^+$ T cells.